




RESEARCH ARTICLE

Study of fog dissipation in an internal boundary layer on Sable Island

Stef L. Bardoel¹  | Sebastian Hoch² | Jesus Ruiz-Plancarte³ | Luc Lenain⁴ |
Ismail Gultepe^{1,5} | Andrey A. Grachev⁶  | Saša Gaberšek⁷  | Qing Wang³ |
Harindra J. S. Fernando^{1,8}

¹Department of Civil and Environmental Engineering and Earth Sciences, University of Notre Dame, Notre Dame, Indiana

²Department of Atmospheric Sciences, University of Utah, Salt Lake City, UT

³Meteorology Department, Naval Postgraduate School, Monterey, California

⁴Scipps Institution of Oceanography, University of California San Diego, La Jolla, California

⁵Engineering and Applied Science and ACE, Ontario Tech University, Oshawa, Ontario Canada

⁶Atmospheric Dynamics & Analytics Branch, DEVCOM Army Research Laboratory, White Sands Missile Range, New Mexico

⁷Marine Meteorology Division, US Naval Research Laboratory, Monterey, California

⁸Department of Aerospace and Mechanical Engineering, University of Notre Dame, Notre Dame, Indiana

Correspondence

Stef L. Bardoel, LEGI, Univ. Grenoble Alpes, CNRS, Grenoble 38000, France.
Email: stef.bardoel@univ-grenoble-alpes.fr

Funding information

Office of Naval Research, Grant/Award Number: N00014-21-1-2296

Abstract

An interesting fog dissipation event was observed during the Fog and Turbulence Interactions in the Marine Atmosphere (FATIMA) Grand Banks field campaign, where a fog-free region appeared immediately downstream of Sable Island as fog advected past it. This fog-free region was predicted a priori by a high-resolution numerical model that guided intensive operational periods of the FATIMA campaign, and its presence was adumbrated by *GOES* satellite observations. A comprehensive set of field observations shows that this fog-free layer was due to the development of a (daytime) thermal internal boundary layer (IBL) that grew with distance from the leading shore line. The net incoming radiation following sunrise led to an increased air temperature and decreased relative humidity close to the ground, thus dissipating fog over the island. The height of the thermal IBL, as identified by the thickness of the superadiabatic layer, was found to be consistent with several available theoretical IBL formulae.

KEYWORDS

coastal zone, fog, internal boundary layers, turbulence

1 | INTRODUCTION

The ability to predict coastal and marine fog accurately is crucial for many applications, such as aviation (Gultepe *et al.*, 2021), marine transportation (Fernando *et al.*, 2021),

and free-space optical communication (Schimmel *et al.*, 2018), yet it is one of the most poorly predicted meteorological phenomena (Pagowski *et al.*, 2004). The direct consequence of fog is a reduction of visibility due to the presence of suspended water droplets and/or ice

crystals close to the Earth's surface (WMO, 1992), and in meteorology it is defined as the reduction of near-surface visibility below 1 km. Water droplets are able to form and grow by the condensation of water vapour on hygroscopic aerosol nuclei, known as fog condensation nuclei (FCN), when the relative humidity (RH) with respect to water is near 100% (Gultepe *et al.*, 2021). Fog is broadly categorized into three types based on the formation mechanism, namely mixing fog, radiation fog, and advection fog (Fernando *et al.*, 2021). "Mixing fog" forms when two near-saturated air masses of different temperatures mix to achieve supersaturation (Bardoel *et al.*, 2021; Rodhe, 1962; Taylor, 1917). "Radiation fog" appears when air over the surface is cooled below the dew point due to net outgoing radiation, usually under clear skies and with low winds (Gultepe *et al.*, 2007). "Advection fog" occurs when warm air flowing over a colder surface is cooled below the dew point (warm fog), or when cold air flowing over a warmer surface is brought to supersaturation by evaporation (cold fog). A combination of the latter two types, advection–radiation fog, is found in coastal regions when moist air from a large body of water advects over land and is radiatively cooled (Ryznar, 1977). More complicated situations are found in nature, for example, the formation of fog-laden layered density structures in a stably stratified atmospheric boundary layer as a result of limited vertical mixing (Fernando *et al.*, 2023). The commonality between these fog types is that they are physically governed by the local FCN concentration, air temperature, and relative humidity (Gultepe *et al.*, 2007; Gultepe & Isaac, 1997).

The predictability of coastal fog is complicated by the spatial inhomogeneity of surface properties between land and ocean (O'Brien *et al.*, 2013). Numerical weather prediction (NWP) models traditionally represent the vertical exchange of momentum, heat, and moisture near the surface using Monin–Obukhov similarity theory (MOST), which assumes spatial homogeneity of surface properties (Kaimal & Finnigan, 1994; Monin & Yaglom, 1971; Sorbjan, 1989; Stull, 1988; Wyngaard, 2010). While this is a reasonable assumption in many cases, it is nominally violated in coastal areas, since inland areas generally have a higher surface roughness and lower heat capacity compared with the ocean, leading to an overall weaker diurnal cycle over the ocean (Grachev *et al.*, 2018). The discontinuity of land/ocean surface properties causes a flow "adjustment" to the new surface conditions as the wind flows over it, which occurs in a growing layer downstream of the discontinuity (leading edge); this is called an internal boundary layer (IBL). Aside from coastal areas, IBLs are commonly formed at the edges of plant, wetland, and urban canopies (Coceal & Belcher, 2004; Mahrt, 2000).

Only a few studies exist on the influence of IBLs on fog. Kim and Yum (2012) studied the formation mechanism of warm fog (cold sea-fog) in the Yellow Sea (YS) numerically, alluding to the influence of a thermal IBL. As warm and moist air advects over a colder sea surface, a stable thermal IBL is formed with decreasing air temperature by radiative cooling and downward turbulent heat fluxes. The dew-point temperature, however, does not decrease as rapidly because of moisture loss due to the downward vapour flux, which to some degree is compensated by moisture advection. This eventually leads to saturation and thus to cold sea fog. Gao *et al.* (2007) present similar findings and found that turbulent mixing by wind shear is also important.

On the other hand, warmer thermal IBLs prompt dissipation of fog, an example being urban clear islands (UCIs), which are local clearings within a larger fog layer in urban areas. UCIs are thought to form due to urban heat islands (UHIs), areas of increased temperatures compared with their surroundings (Sachweh & Koepke, 1995). Lee (1987) confirmed the presence of UCIs near several cities during a fog event in the California Central Valley using satellite observations and local visibility measurements. Sachweh and Koepke (1995) reported several UCIs related to the UHI phenomenon in southern Germany and the Po Valley. Underwood and Hansen (2008) showed that the area and shape of UCIs near Fresno, California vary significantly between individual events. Gautam and Singh (2018) correlated the size of UCIs with the total population of urban areas. Yan *et al.* (2020) reproduced a radiation-fog event in eastern China using numerical simulations, including UCIs.

This work was motivated by observations made during the first field campaign of the Fog and Turbulence Interactions in the Marine Atmosphere (FATIMA) project conducted in the Grand Banks (GB) area, North Atlantic in July, 2022 (FATIMA–GB). This included 14 land-based intensive operational periods (IOPs) on one of the research sites, Sable Island (SI), a small isolated islet in the southern part of the GB area. During the daily weather forecasting meetings, an interesting fog event was predicted for IOP10 (1800 ADT, July 23, 2022–1200 ADT, July 25, 2022, where Atlantic Daylight Time (ADT) = UTC – 3 h) by the Coupled Ocean/Atmosphere Mesoscale Prediction System (COAMPS[®], Hodur, 1997), where a fog-free region appeared directly downwind of SI in an otherwise large extent of fog surrounding the islet, very similar to a UCI, which could be called a "fog shadow" (similar to a "rain shadow"). Gaberšek *et al.* (2024) provide a more extensive introduction to the phenomenon, introducing the name "fog shadow" and results from COAMPS[®]. Model details are discussed further by Fernando *et al.* (2024). This study

focuses on the genesis of the fog shadow on SI, which was hypothesized to be due to a thermal IBL emanating at the ocean–land discontinuity, wherein

- (I) an increase of temperature (T) and consequent reduction in RH lead to the daytime dissipation of the fog, and/or
- (II) intense turbulence due to shear and/or buoyancy production in the IBL may have helped dissipate the fog.

Note that another IBL is formed at the lee edge of the island (land–ocean discontinuity, e.g., see Figure 1b), but the focus here is on the IBL originating from the leading ocean–land discontinuity. In this article, FATIMA–GB observations are used to confirm the presence of fog dissipation in a shallow layer near the surface over the island, which is likely linked to the fog shadow downstream. Section 2 describes the basics of IBL theory. Section 3 gives an overview of the SI terrain and instrumentation. Observations are presented in Section 4, and Section 5 investigates the role of the IBL in relation to the fog shadow. Additionally, an estimation of IBL height over SI and comparison with theoretical expressions are presented. Section 6 presents a brief discussion and the conclusions are given in Section 7.

2 | INTERNAL BOUNDARY-LAYER THEORY

Often the classical IBL problem is considered in a simplified configuration where two homogeneous semi-infinite surfaces meet at a straight-line discontinuity. This allows a two-dimensional treatment of the problem, as shown in Figure 1. Upstream of the discontinuity the flow is in equilibrium, governed by the upstream momentum surface-roughness length z_{0U} and other surface properties such as the thermal roughness length z_T , pressure gradient driving the flow (or the surface friction velocity), and surface fluxes of heat and moisture. The IBL height $h(x)$ originating at the leading edge grows downstream with distance x (or fetch). The processes governing this initial growth are not fully understood, as reviewed by Krishnamurthy *et al.* (2023). Nevertheless, the presence of both an equilibrium layer adjacent to the ground downstream of the discontinuity and a transition layer aloft that merges with the undisturbed flow (Figure 1a) has been confirmed by laboratory experiments and numerical simulations (Savelyev & Taylor, 2005). The combined equilibrium and transition layers form the IBL.

Table 1 gives an overview of selected formulae that quantify the IBL height h as a function of the fetch x . In pioneering work, Elliott (1958) used momentum and

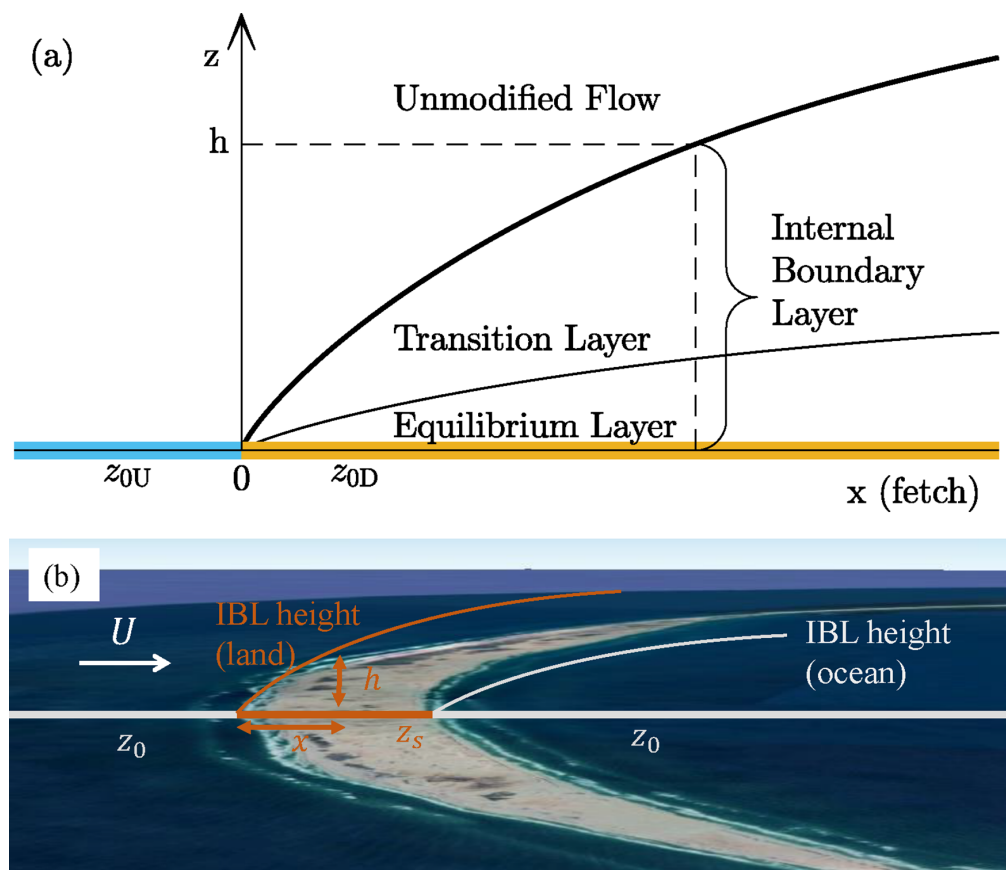


FIGURE 1 A schematic of (a) the development of a 2D internal boundary layer due to a change of surface roughness and (b) the internal boundary-layer configuration for Sable Island. [Colour figure can be viewed at [wileyonlinelibrary.com](https://onlinelibrary.wiley.com)]

TABLE 1 A list of several IBL height formulae for short fetches, adopted from Savelyev and Taylor (2005). The IBL height is h and the fetch is x , z_0 is the surface-roughness length, κ the von Kármán constant, and L the Obukhov length. The subscripts U and D refer to the upstream and downstream regions respectively.

Formula	Author(s)	Notes
$\frac{h}{z_0} = (0.75 - 0.03M) \left(\frac{x}{z_0}\right)^{0.8}$	Elliott (1958)	$M = \ln \frac{z_{0D}}{z_0}$
$2\kappa^2 x = h \ln \frac{h}{z_0}$	Townsend (1965)	$h_0 = h(x = 0)$
$1.73\kappa \frac{x}{z_0} = \frac{h}{z_0} \left(\ln \frac{h}{z_0} - 1 \right) - \frac{h_0}{z_0} \left(\ln \frac{h_0}{z_0} - 1 \right)$	Miyake (1965)	
$\kappa^2 x = h \frac{\ln \frac{h}{z_0} (\ln \frac{h}{z_0} + M)}{2 \ln \frac{h}{z_0}}$	Townsend (1966)	
$\frac{dh}{dx} = \kappa^2 \frac{h}{z_0} \frac{\ln^2 \frac{h}{z_0} + \ln \frac{h}{z_0} \ln \frac{h}{z_0 D}}{F(h) \ln \frac{h}{z_0 U}}$	Radikevitch (1971)	
$1.5\kappa \frac{x}{z_0} = \frac{h}{z_0} \left(\ln \frac{h}{z_0} - 1 \right) \frac{1.03}{z_0}$	Panofsky (1973)	$z_{0r} = \max(z_{0D}, z_{0U})$
$\frac{h}{z_0} = 0.095 \left(\frac{x}{z_0}\right)^{0.8}$	Schofield (1975)	
$0.75\kappa \frac{x}{z_0} = \frac{h}{z_0} \left(\ln \frac{h}{z_0} - 1 \right) - \frac{h_0}{z_0} \left(\ln \frac{h_0}{z_0} - 1 \right)$	Jackson (1976)	$z'_0 = \sqrt{\frac{z_{0D}^2 + z_{0U}^2}{2}}$
$\frac{h}{z_0} = 0.28 \left(\frac{x}{z_0}\right)^{0.8}$	Wood (1982)	$z_{0r} = \max(z_{0D}, z_{0U})$
$\frac{h}{z_0} = 0.28 \left(\frac{x}{z_0}\right)^{0.8}$	Pendergrass and Arya (1984)	
$2.25\kappa \frac{x}{z_0} = \frac{h}{z_0} \left(\ln \frac{h}{z_0} - 1 \right) + 1$	Panofsky and Dutton (1984)	
$h \left(\ln \frac{h}{z_0} - 1 \right) = 1.25\kappa(1 + 0.1M)x$	Savelyev and Taylor (2001)	
$h \left(\ln \frac{h}{\sqrt{z_{0D} z_0}} - 1 \right) = 0.5x$	Savelyev & Taylor (2005, Eq. (28))	
$\left[\ln \frac{h}{z_0} - \psi_m \left(\frac{h}{L_U} \right) \right] \frac{dh}{dx} = A_1 \kappa \frac{z_{0D}}{u_{*U}} + A_2 \frac{h}{x} \left[\ln \frac{z_{0D}}{z_0} - \psi_m \left(\frac{h}{L_U} \right) + \psi_m \left(\frac{h}{L_D} \right) \right]$	Savelyev & Taylor (2005, Eq. (36))	$A_1 = 1, A_2 = 0.5$
$\frac{3}{2} \left(\frac{h}{L_U} \right)^{\frac{3}{5}} \ln \frac{h}{z_0} - \frac{9}{4} \left(\left(\frac{h}{L_U} \right)^{\frac{2}{3}} - \left(\frac{z_{0U}}{L_U} \right)^{\frac{2}{3}} \right) = B\gamma \frac{x}{L_U}$	Krishnamurthy <i>et al.</i> (2023)	$B = 0.28, \gamma = \left(1 + \frac{1}{\alpha^2} \frac{q_0 L_U}{u_*^2} \right)^{1/3}$

Only valid for rough-to-smooth transition

entrainment considerations along with logarithmic mean velocity profiles to estimate the IBL height. Later work used minor differences, such as altered coefficients (Pendergrass & Arya, 1984; Schofield, 1975), different scaling arguments, or empirical data (Hanna, 1987). For example, Wood (1982) and Panofsky (1973) argued that the IBL growth depends only on the characteristics of the rougher surface. Miyake (1965) used a different approach by modelling the vertical propagation of surface change effects as due to turbulent diffusion, which can be expressed as

$$\frac{dh}{dt} = \frac{\partial h}{\partial t} + U(h) \frac{\partial h}{\partial x} = A\sigma_w, \quad (1)$$

where σ_w is the standard deviation of the vertical velocity component, $U(h)$ the mean wind speed at height h , and A a proportionality constant. Furthermore, Miyake (1965) assumed a horizontal velocity $U(z) = u_{*D}/\kappa \ln(z/z_{0D})$, $\sigma_w/u_* = \text{constant}$, and steady-state conditions ($\partial h/\partial t = 0$) to model the IBL. Here, u_{*D} is the downstream friction velocity, z the vertical coordinate, and κ the von Kármán constant. The majority of expressions in Table 1 assume that IBLs are the same for rough-to-smooth and smooth-to-rough transitions, but Antonia and Luxton (1971, 1972) noted clear differences between the cases. The IBL growth of the smooth-to-rough case is predominantly due to turbulence generated at the discontinuity, whereas the rough-to-smooth case is dominated by turbulence from the upstream (rougner) surface within the boundary layer. Krishnamurthy *et al.* (2023) used this observation to derive an expression specific to the rough-to-smooth case, using the upstream characteristic horizontal integral length \mathcal{L}_U and standard deviation of the horizontal velocity σ_u as additional parameters. They also included the effects of convective turbulence in the downstream region. If the downstream surface is warm enough, σ_w is increased due to downstream convective turbulence, which was parameterized as (Deardorff, 1983)

$$\sigma_w^3 = (\sigma_{wm})^3 + (\alpha w_*)^3 = (\sigma_{wm})^3 + \alpha^3 q_0 h_1, \quad (2)$$

where σ_{wm} is the contribution of mechanical turbulence (shear production), αw_* the contribution through convection, $w_* = (q_0 h_1)^{1/3}$ the convective velocity, q_0 the buoyancy flux, and h_1 the local ABL height. The constant α is usually taken as unity (Deardorff, 1983), but Adrian *et al.* (1986) showed that in practice $\alpha = 0-0.7$ depending on the value of z/h_1 . The only other expression that includes buoyancy effects is that of Savelyev & Taylor (2005, Eq. (36)), who use a stability correction function $\psi_m(\zeta) = \int_0^\zeta (1 - \phi_m(\zeta)) d\zeta/\zeta$. Here $\phi_m(\zeta)$ is a Monin–Obukhov universal similarity function of wind

shear and

$$\zeta = \frac{z}{L} = \frac{\kappa g z}{\theta_v} \frac{\overline{w' \theta_v'}}{u_*^3} \quad (3)$$

is the stability parameter, L the Obukhov length, g gravitational acceleration, w the vertical velocity, θ_v the virtual potential temperature, and the overbar and prime denote the mean and deviation from the mean, respectively. Common expressions for the unstable and stable case are (Kaimal & Finnigan, 1994)

$$\phi_m(\zeta) = \begin{cases} (1 + 16\zeta)^{-1/4}, & -2 \leq \zeta \leq 0, \\ (1 + 5\zeta), & 0 \leq \zeta \leq 1. \end{cases} \quad (4)$$

Similarly, the standard deviation of the vertical velocity component in convective turbulence was parameterized using MOST as

$$\frac{\sigma_w}{u_*} = \phi_w(\zeta) = \begin{cases} 1.25(1 - 3\zeta)^{1/3}, & -2 \leq \zeta \leq 0, \\ 1.25(1 + 0.2\zeta), & 0 \leq \zeta \leq 1. \end{cases} \quad (5)$$

In other expressions, such as Miyake (1965), the ratio σ_w/u_* is assumed to be constant within the IBL.

3 | INSTRUMENTATION

Two field campaigns have been conducted as part of FATIMA, the first of which was conducted in the GB area in the Northern Atlantic (FATIMA–GB: July 1–31, 2022) and is the focus here. The second (FATIMA–YS) took place in the Yellow Sea off the coast of South Korea during June 20–July 9, 2023. The GB campaign involved measurements on SI, aboard an instrumented research vessel (R/V *Atlantic Condor*), a set of Wave Gliders, and at the Hibernia oil platform. The fog–climatology-based site selection and the details of the FATIMA field program, including IOPs, are given in Fernando *et al.* (2024). The information given below is relevant to IOP 10 only.

Figure 2a,b provides an overview of SI, located roughly 300 km to the east of Halifax, Nova Scotia. It is a narrow, crescent-shaped sandbar, being approximately 40 km long and 1.2 km wide at its widest point. The island is flat with elevations generally below 10 m above sea level (ASL), with the highest point at 30 m ASL. Roughly 50% of the island is covered in vegetation (12% heath, 37% grassland, 2% sandwort), and the remainder in sand and ponds (Colville *et al.*, 2016). Additionally, the island is home to about 500 horses, the largest breeding colony of grey seals, and several large bird colonies.

The SI site consisted of three auxiliary sites centred around three heavily instrumented meteorological

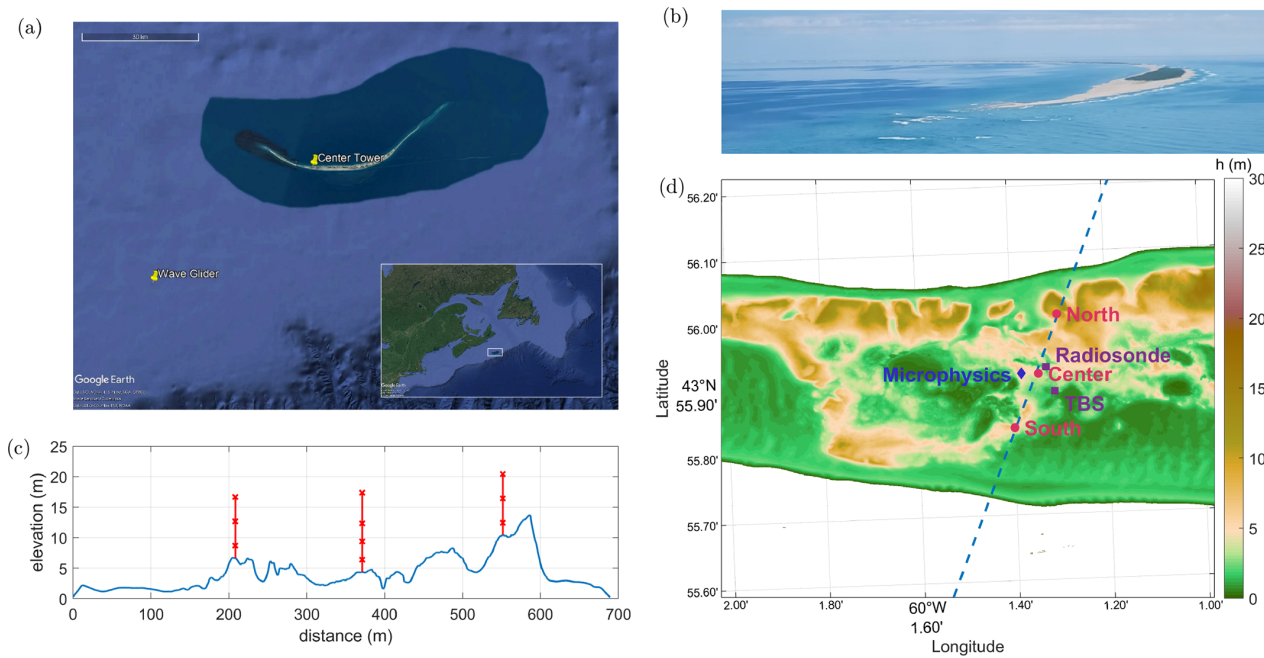


FIGURE 2 Overview of Sable Island, with (a) a Google Earth photo of Sable Island with the location of the centre tower and a Wave Glider on July 24, 2022, (b) aerial view of Sable Island, (c) transect of the elevation of Sable Island at the three towers measured from the southern coast, and (d) digital elevation map of Sable Island near the three towers. The elevation data in (c) and (d) were taken from the Canadian High Resolution Digital Elevation Model, which has a horizontal resolution of 1 m. The red lines and crosses in (c) denote the location of the three towers and the individual levels, respectively. The exact location of the transect is denoted by the dashed blue line in (d). [Colour figure can be viewed at wileyonlinelibrary.com]

flux towers, located on the western part of the island (Figure 2a,d). The elevation data are taken from the Canadian High-Resolution Digital Elevation Map (HRDEM), based on 1-m resolution topographic elevation data derived from airborne LiDAR measurements. The towers were positioned into the dominant wind direction, thereby providing a south–southwest to north–northeast transect of the island (Figure 2d). The towers were appropriately named south, centre, and north tower, respectively. Overall, the elevation changes across the transect were relatively minor (Figure 2c). A summary of the instrumentation on SI used in this article is given in Table 2.

The most densely instrumented was the area surrounding the centre tower (4.4 m ASL). This 15-m tower was equipped with four levels (2, 5, 8, and 13 m above ground level, AGL) of instrumentation (Figure 3a), each level having a fast-response ultrasonic anemometer (Campbell Scientific IRGASON at level 1, RM Young 81000 at levels 2–4) for velocity and virtual potential temperature measurements at 20 Hz and slow-response temperature and relative humidity (T/RH) measurements at 1 Hz (Vaisala HMP155). The IRGASON also recorded water-vapour fluxes. The visibility was measured using several Present Weather Detectors (PWDs: Campbell Scientific CS125 at levels 1, 3, and Campbell Scientific CS120 for level 4), with data taken every 10 seconds. Other details

of tower turbulence measurements, data processing, and data-quality criteria during FATIMA–GB are similar to those described by Grachev *et al.* (2018, 2021).

Longwave in- and outgoing radiative fluxes were measured using Kipp and Zonen CGR4 pyrgeometers at 2 m height on a sawhorse structure and at 13 m height on the centre tower (Figure 3a,c). The sawhorse also contained two pyranometers (CMP21, Kipp and Zonen) for incoming and outgoing shortwave radiation measurements. Additionally, measurements of the soil heat flux (HFP01SC, Hukseflux), average soil temperature (TCAV, Campbell Scientific), and soil moisture content (CS655, Campbell Scientific) were made.

A microphysics supersite (Gultepe *et al.*, 2019) was placed approximately 50 m to the west of the centre tower (Figure 3b). It was instrumented with a PWD (Vaisala PWD52) for visibility and precipitation measurements, an ultrasonic anemometer (RM Young 81000), and an SPN1 radiometer (Delta-T Devices Ltd) for direct and diffuse SW radiation measurements. A fog measuring device (DMT FM-120) provided droplet spectral measurements (1–50 μm). There also was a ceilometer (Vaisala CL51) for vertical profiles of optical backscatter.

The south tower (6.6 m ASL) was equipped with three levels (2, 6, and 10 m AGL) of instrumentation, each level having a fast-response ultrasonic anemometer

TABLE 2 Summary of the instrumentation on Sable Island. Only the instrumentation used in this article is listed. The location of the sites is given in Figure 2d.

Instrument	Site	Height	Variables
Vaisala CL31 ceilometer	South tower	0 m AGL	backscatter
Vaisala PWD22	South tower	2 m AGL	visibility
CS IRGASON	Centre tower	2 m AGL	wind speed, temperature, water vapour
RM Young 81000 ultrasonic anemometer	Centre tower	5, 8, 13 m AGL	wind speed, temperature
Vaisala HMP 155 T/RH probe	Centre tower	2, 5, 8, 13 m AGL	temperature, RH
CS125 present weather detector	Centre tower	2, 8 m AGL	visibility
CS120 present weather detector	Centre tower	13 m AGL	visibility
Kipp and Zonen CMP21 pyranometer	Centre tower	2 m AGL	SW radiation
Kipp and Zonen CGR4 pyrgeometer	Centre tower	2, 13 m AGL	LW radiation
Hukseflux HFP01SC soil heat-flux plate	Centre tower	−0.05 m AGL	ground heat flux
CS TCAV soil temperature probe	Centre tower	−0.05 to 0 m AGL	soil temperature
DMT FM-120	Microphysics tower	1 m AGL	droplet spectra
Vaisala PWD52 present weather detector	Microphysics tower		visibility
Vaisala CL51 ceilometer	Microphysics tower	0 m AGL	backscatter
Vaisala CL31 ceilometer	North tower	0 m AGL	backscatter
Vaisala PWD22 present weather detector	North tower	2 m AGL	visibility
Vaisala RS41–SGP rawinsondes	Radiosonde	0 to 5000 m ASL	wind speed, temperature, RH, pressure
Tethered balloon system	TBS	0 to 100 m AGL	wind speed, temperature, RH, pressure

(RM Young 81000) for velocity and virtual potential temperature measurements at 20 Hz and slow-response T/RH measurements at 1 Hz (Rotronic HygroClip 2). Vertical profiles of backscatter were recorded with a Vaisala CL31 ceilometer. A single Streamline XR Doppler lidar (HaloPhotonics) conducted co-planar range–height indicator scans to measure winds and aerosol backscatter. The north tower (10.4 m ASL) was also equipped with three levels (2, 6, and 10 m AGL), each instrumented with RM Young 81000 ultrasonic anemometers and Campbell Scientific EE181 T/RH probes. Also located at the site was a Vaisala CL31 ceilometer.

Vertical meteorological profiles were obtained using (i) Vaisala radiosondes that recorded the wind speed (U), wind direction, temperature (T), and relative humidity at 1 Hz using RS41–SGP rawinsondes (Vaisala MW41 sounding system) and (ii) a tethered balloon system (TBS: same variables plus attached up- and down-facing gimbed pyrgeometers (Apogee SL-510/610) and optical particle counter (Alphasense OPC-N3)). Radiosondes were released 30 m to the northeast of the centre tower and the TBS was operated about 70 m to the southeast of the centre tower (Figure 2d). The maximum TBS altitude was limited to 100 m AGL due to high wind speeds. During IOP10, a total of 15 radiosondes were released. The TBS

was operated on July 24 during 1315–1900 ADT, during which a total of 26 vertical profiles were obtained.

Measurements upstream of SI were provided by an SV3 Liquid Robotics Wave Glider (WG: Figure 3d). It was instrumented with a Vaisala WXT530 and an Airmar 200WX for wind speed, wind direction, air temperature, and relative humidity measurements. Water conductivity–temperature–depth (CTD) measurements were recorded using a Sea-Bird Electronics Glider Payload CTD (GPCTD) sensor. Additional high-frequency velocity measurements were taken with a Gill R3-50 ultrasonic anemometer at 1 m ASL. For more details about the Wave Glider, including additional instrumentation, see Lenain and Melville (2014) and Grare *et al.* (2021). During IOP10, the glider was located about 50 km to the southwest of SI (Figure 2a), generally upwind of the island.

4 | FOG OBSERVATIONS DURING IOP10

Around noon on July 23, 2022, the winds measured from the centre tower were southwesterly, about $5 \text{ m} \cdot \text{s}^{-1}$, with RH of about 90–93% and $T = 18\text{--}19^\circ\text{C}$ (Figure 4). Conditions were clear, with visibility close to 10 km until

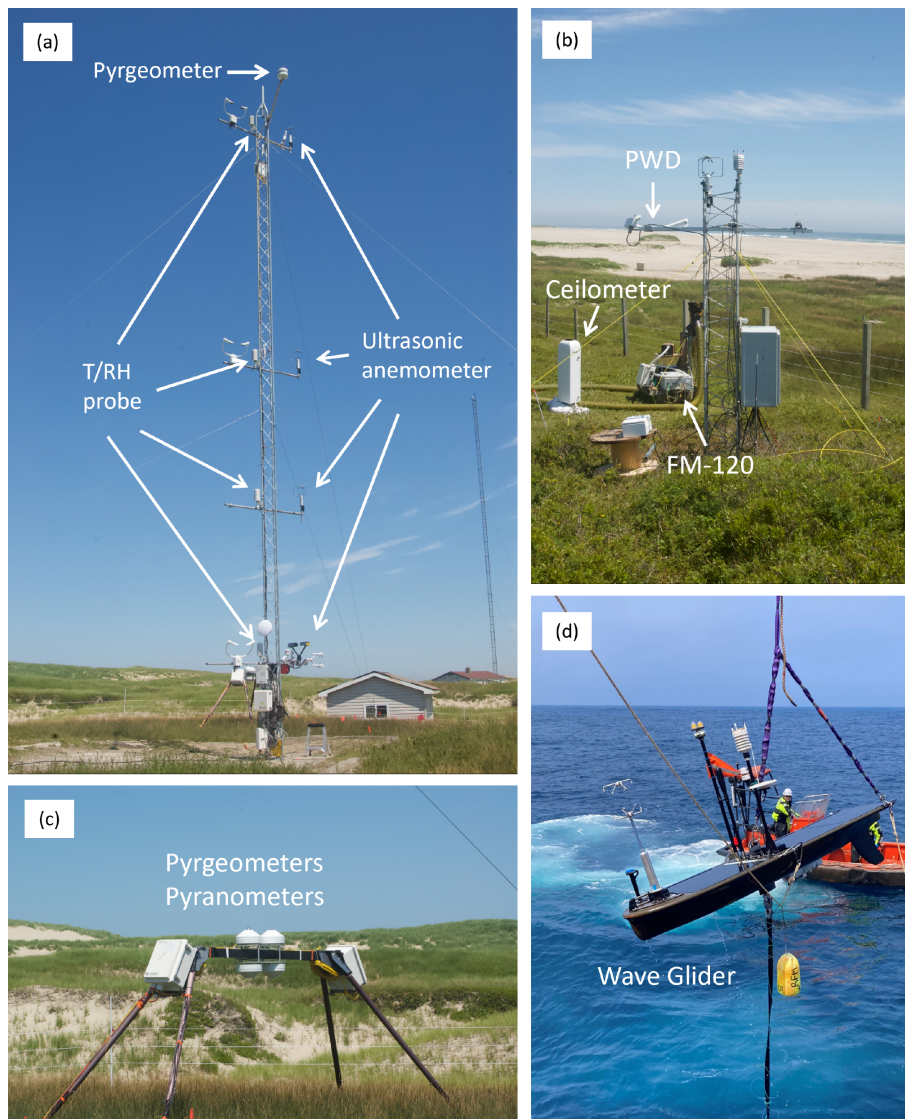


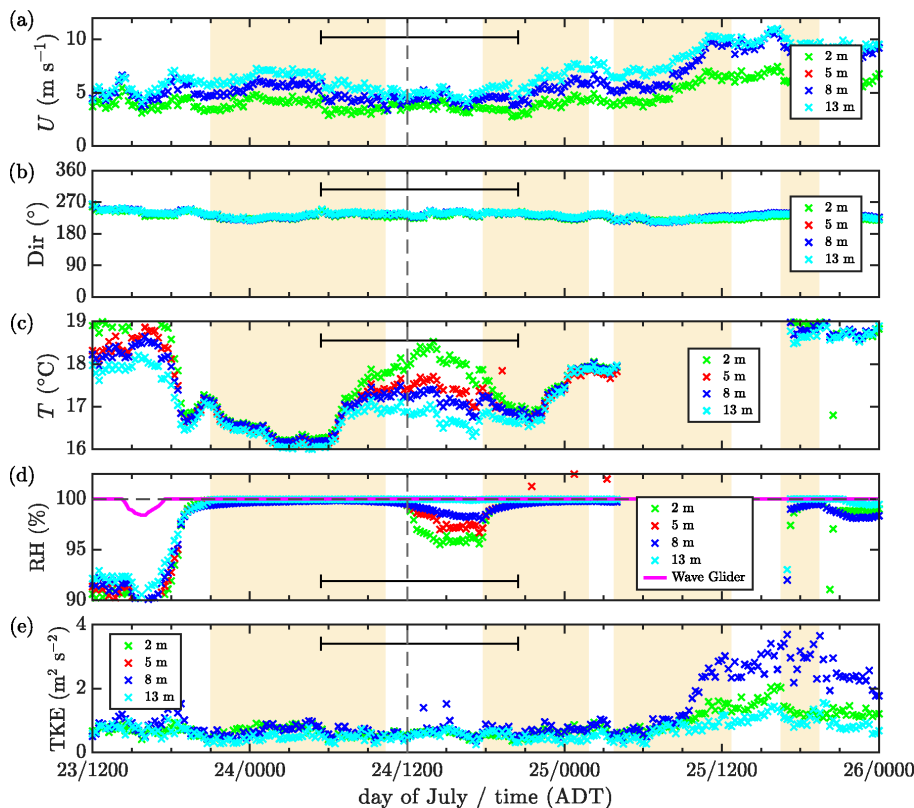
FIGURE 3 Instrumentation of the (a) the centre tower, (b) microphysics supersite, (c) radiation sawhorse, and (d) Wave Glider used during FATIMA-GB. Details of the instrumentation are given in the text. [Colour figure can be viewed at [wileyonlinelibrary.com](https://onlinelibrary.wiley.com/doi/10.1002/qj.4891)]

1845 ADT, when the visibility suddenly dropped below 1 km and fog appeared (Figure 5a). The visibility generally remained around 300 m until 1030 ADT the next day, several hours after sunrise on July 24. The ceilometer backscatter confirms the sudden onset of a fog layer with a thickness of 100 m (Figure 5e). Satellite observations (not shown) show that fog was advected from the southwest toward SI. Unfortunately, the fog monitor FM-120 was malfunctioning during the fog onset, but it clearly indicated an increase in the median volume diameter (MVD: Figure 5b), droplet number concentration N_d (Figure 5c), and liquid water content (LWC: Figure 5d) sometime after the fog genesis. These conditions persisted until about 1030 ADT on July 24, whereupon the visibility increased significantly, fluctuating in the 1–2 km range (usually identified as “mist”). At this time, the FM-120 recorded a slight drop in the droplet MVD, a significant decrease in the droplet number density, and a striking drop of LWC (Figure 5b–d). The magnitude of backscatter in a surface

layer of thickness 25 m decreased (Figures 5e, 6a–c), although remaining unchanged at greater heights. The reduction of backscatter is more evident at the centre and north tower (Figure 6b,c, onset at 1030 ADT), with stronger reductions up to 25 m AGL during the day. This possibly indicates that at the south tower the height of the layer with reduction of backscatter was lower than the ceilometer vertical resolution (10 m), since the PWD at the south tower (2 m AGL, Figure 6e) was still able to register an increase of visibility.

All ceilometers observed a momentary lifting of the fog from the surface just before 1800 ADT. The duration of the period of improved visibility (mist) lasted for about nine hours, after which fog returned for the rest of the night (Figure 6a–e). The visibility at 8 m of the centre tower is somewhat lower than that at 2 m (measured using similar instruments), but both levels showed the same visibility trends (Figure 6d). Overall, the daytime visibility improvement at lower altitudes, particularly at the centre

FIGURE 4 Time series of (a) wind speed, (b) wind direction, (c) temperature, (d) relative humidity, and (e) TKE. The shaded regions correspond to foggy conditions. The dashed lines indicate the initial appearance of the fog shadow. On July 24, sunrise and sunset occurred at 0525 ADT and 2028 ADT, respectively, which is indicated by the black horizontal line. The data were collected from the centre tower during IOP10 with upstream relative humidity measured by the waveglider. The wind speed, wind direction, and turbulence statistics are calculated from 15-min averaged 20-Hz ultrasonic anemometer measurements. Temperature and relative humidity were measured using 1-Hz T /RH sensors. The ultrasonic anemometer at 5 m AGL was malfunctioning during IOP10 and therefore no velocity data are available at 5 m AGL in the figure. [Colour figure can be viewed at wileyonlinelibrary.com]



and north towers (Figure 6a–c) noted above, suggests that (surface) ground effects that come into play during the advection of fog-laden air over SI may be responsible for the visibility increase. At the south tower, the fog layer mostly persisted during the entire day, with minor reductions in backscatter close to the surface during the day (Figure 6a).

Figure 7 shows the brightness-temperature difference (BTD) between the 10.35- μm infrared (IR) and 3.9- μm shortwave infrared (SWIR) bands as recorded by the *GOES-18* satellite, which can be used to (roughly) identify the presence of smaller water droplets (and hence fog or stratus) in the lower atmosphere (Amani *et al.*, 2020). While BTD inferences are not fully applicable during daytime because of a shortwave-radiation impact on the 3.9- μm SWIR channel (Gultepe *et al.*, 2021), a careful inspection of the data and a comparison with red-band (0.64- μm) observations allows us to glean some information on the presence of fog. SI (marked in red) is clouded with fog (BTD ≈ 10 K) at 1100 ADT on July 24 (Figure 7a; also Figure 6d,e). After 1200 ADT, a region with improved visibility started to appear to the northeast of SI, in the island “shadow” (BTD ≈ 0 K). During the entire IOP10, the winds were southwesterly (Figure 4b), and therefore the region of improved visibility downstream of SI could be considered as a “fog shadow” (see Gaberšek *et al.* (2024) for a discussion), which extended for 30 km downstream.

At 1300 ADT the fog shadow ended temporarily, with fog appearing again immediately downstream of SI (Figure 7c). The remaining (shrinking) patch of improved visibility moved further downstream of the SI, completely disappearing at 1400 ADT. Roughly at the same time, a second fog shadow appeared (Figure 7d–f), which grew streamwise and reached a maximum length of about 80 km. The end of this second fog shadow could not be captured because of blocking of view by a cloud layer. Most likely, this fog shadow would have started disappearing at 1800 ADT, when the visibility on the island decreased below 1 km indicating fog (Figure 6e), and the remaining fog-free patch would disappear sometime later. The ceilometer observations close to the surface (Figure 6a–c) showed an increase of backscatter close to the surface at this time, indicating the reappearance of fog.

In all, the tower data in Figure 4 and backscatter and visibility data in Figure 6 confirm that fog dissipation started close to the surface of SI and eventually pierced through the fog layer to improve visibility in a thin layer near the ground. This thin “dissipative” layer was dominated by mechanical turbulence, with smaller contribution from convective turbulence, which could be seen from the lack of a diurnal trend in the turbulence kinetic energy (TKE: Figure 4e). Evidence for the lack of contribution of thermal (convective) forcing to the TKE is given in Section 5.1. The fog dissipation was abetted by increasing

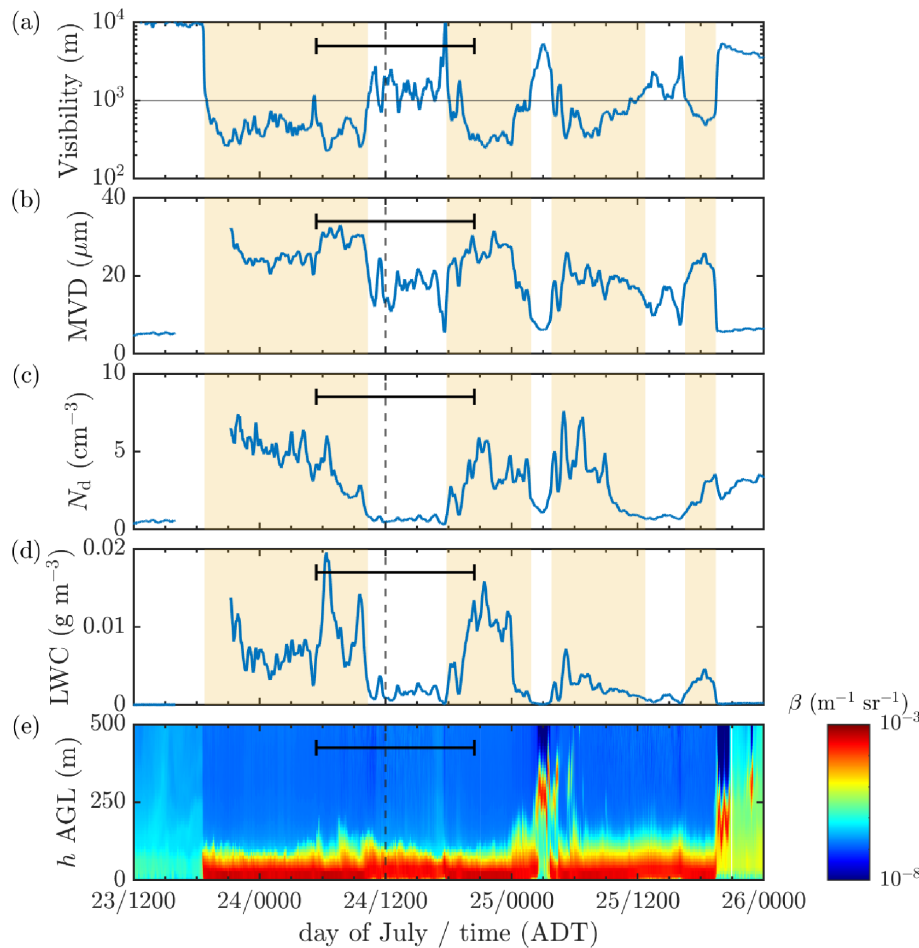


FIGURE 5 Time series of (a) visibility, (b) mean volume diameter, (c) droplet number density, (d) liquid water content, and (e) ceilometer backscatter (β) profiles at the microphysics supersite near the centre tower during IOP10. The shaded regions correspond to foggy conditions. The dashed lines indicate the initial appearance of the fog shadow. On July 24, sunrise and sunset occurred at 0525 ADT and 2028 ADT, respectively, which is also indicated by a black horizontal line. A second solid horizontal line in (a) represents the fog definition threshold. The visibility was measured with a present weather detector (PWD), the backscatter profile with a ceilometer, and the other variables were measured with an FM-120. [Colour figure can be viewed at [wileyonlinelibrary.com](https://onlinelibrary.wiley.com/doi/10.1002/qj.4891)]

temperature and hence decreasing RH and surface stability. As such, the “fog shadow” in this case is governed by the advection of the fog layer over SI and the ocean downstream. A summary of the fog observations is given in Table 3. Section 5 aims to characterize the IBL on SI and a summary of the fog and IBL observations is given in Section 5.1.

5 | INTERNAL BOUNDARY-LAYER OBSERVATIONS

As discussed in Section 4, the dissipation of marine fog over SI and concomitant generation of a “fog shadow” downstream of SI was a highlight of IOP10. As noted, the timing of the fog shadow and the concurrent fog dissipation over SI suggest that the fog shadow was related to the IBL forming over SI due to daytime heating of the ground. In this section, we explore the formation of IBLs over SI, which includes a comparison of upstream (ocean) and downstream (SI) surface conditions, inspection of vertical meteorological profiles, and comparison of measured IBL heights with available theoretical expressions.

5.1 | Comparison of offshore and onshore surface conditions

The ocean conditions were recorded by the Wave Glider (50 km upstream of SI) and conditions on SI by instrumentation surrounding the centre tower. The fluxes on SI were calculated using traditional eddy-covariance methods according to

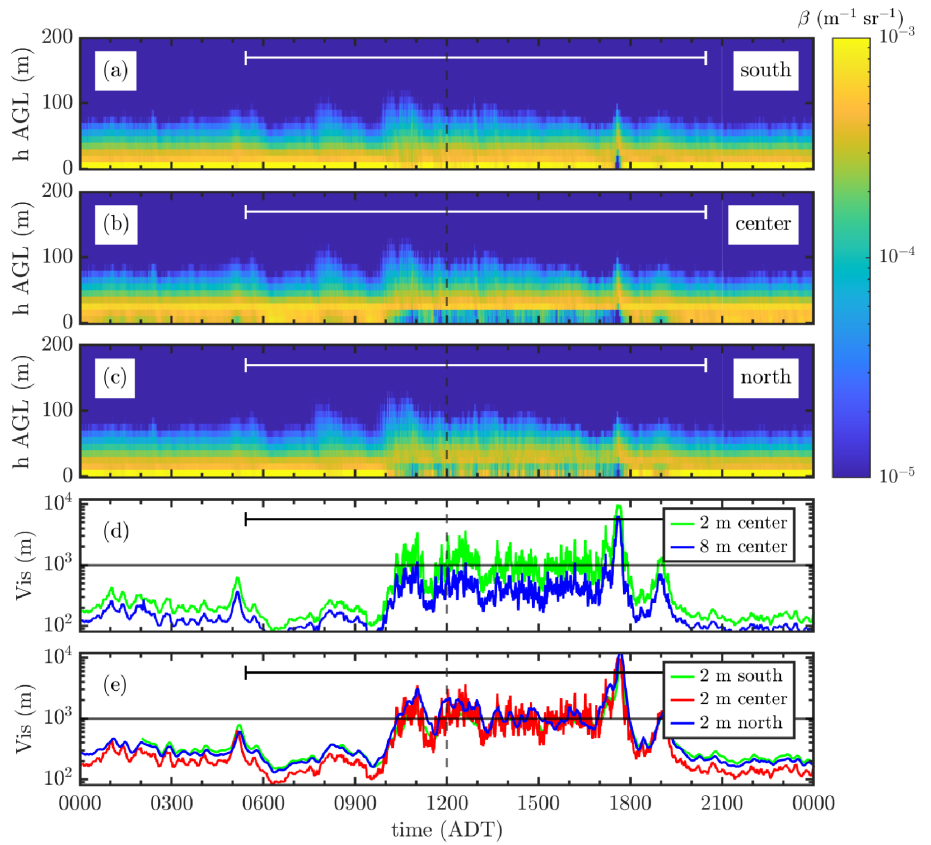
$$u_* = \sqrt{-\overline{u'w'}}, \quad (6)$$

$$H = \rho c_p \overline{w'\theta'}, \quad (7)$$

$$\lambda E = \rho \lambda \overline{w'q'}, \quad (8)$$

where H is the sensible heat flux, λE the latent heat flux, u and w are the streamwise and vertical velocities, c_p is the specific heat capacity of air at constant pressure, ρ the mean air density, λ the latent heat of evaporation of water, θ the potential temperature of air, and q the specific humidity of air. These fluxes are assumed constant within the surface layer, leading to a classical logarithmic

FIGURE 6 Ceilometer backscatter (β) observations at the (a) south tower, (b) microphysics supersite near the centre tower, and (c) north tower, (d) visibility at the centre tower, and (e) 2-m visibility at the south, centre, and north tower on July 24, 2022. Note that the limits of the colour bar used here differ from those of Figure 5e, which was necessary to observe the reduction of backscatter close to the surface more clearly in this figure. The dashed lines indicate the initial appearance of the fog shadow. On July 24, sunrise and sunset occurred at 0525 ADT and 2028 ADT, respectively, which is indicated by the black (or white) horizontal line. The additional solid horizontal lines in (d,e) represent the fog definition threshold. [Colour figure can be viewed at wileyonlinelibrary.com]



velocity profile:

$$U(z) = \frac{u_*}{\kappa} \left(\ln \frac{z}{z_0} - \psi_m(\zeta) \right), \quad (9)$$

where $\psi_m(\zeta)$ is a stability correction function (see Equations 3 and 4). The surface roughness of SI was estimated by using Equation (9) with the 2-m wind speed, friction velocity u_* , and stability parameter ζ , assuming that MOST is valid, although a nearby land–ocean discontinuity (horizontal inhomogeneity) is present.

For the oceanic conditions, bulk parameterizations were employed, and the surface-roughness length and friction velocity were estimated by solving Equation (9) together with Charnock's Charnock's (1955). expression:

$$z_0 = 0.011 \frac{u_*^2}{g} + 0.11 \frac{\nu}{u_*}, \quad (10)$$

where ν is the kinematic viscosity of water and the extra term $0.11\nu/u_*$ is the smooth flow limit, following Smith (1988). The sensible heat flux was calculated using

$$H = \rho c_p C_h U(z) (\theta_0 - \theta(z)), \quad (11)$$

where $\theta(z)$ is the potential temperature at height z and θ_0 the aerodynamic potential temperature. Typically, θ_0

is obtained by integrating the nondimensional temperature gradient vertically from some level in the surface layer down to the thermal roughness length z_T . Given the unavailability of such temperature profiles, θ_0 was assumed to be equal to the sea-surface temperature (SST). The heat transfer coefficient C_h is calculated using

$$C_h = \frac{\kappa}{\ln(z/z_0) - \psi_m(\zeta)} \frac{\kappa}{\ln(z/z_T) - \psi_h(\zeta)}, \quad (12)$$

where $\psi_h = \int_0^\zeta (1 - \phi_h(\zeta)) d\zeta / \zeta$ is a stability function based on the universal function ϕ_h for thermal stratification. Given z_T is unknown, it was set equal to the momentum roughness length (Mahrt & Vickers, 2004). The universal function for temperature is (Kaimal & Finnigan, 1994)

$$\phi_h(\zeta) = \begin{cases} (1 + 16\zeta)^{-1/2}, & -2 \leq \zeta \leq 0, \\ (1 + 5\zeta), & 0 \leq \zeta \leq 1. \end{cases} \quad (13)$$

The values of H and ζ were calculated iteratively using Equations (11) and (12) until a convergence was reached. Neutral conditions ($\zeta = 0$) were assumed at the initialization.

Figure 8 gives surface flow characteristics over the ocean (using the Wave Glider) and SI (instruments in the centre tower area). The 1-m wind speed over the ocean

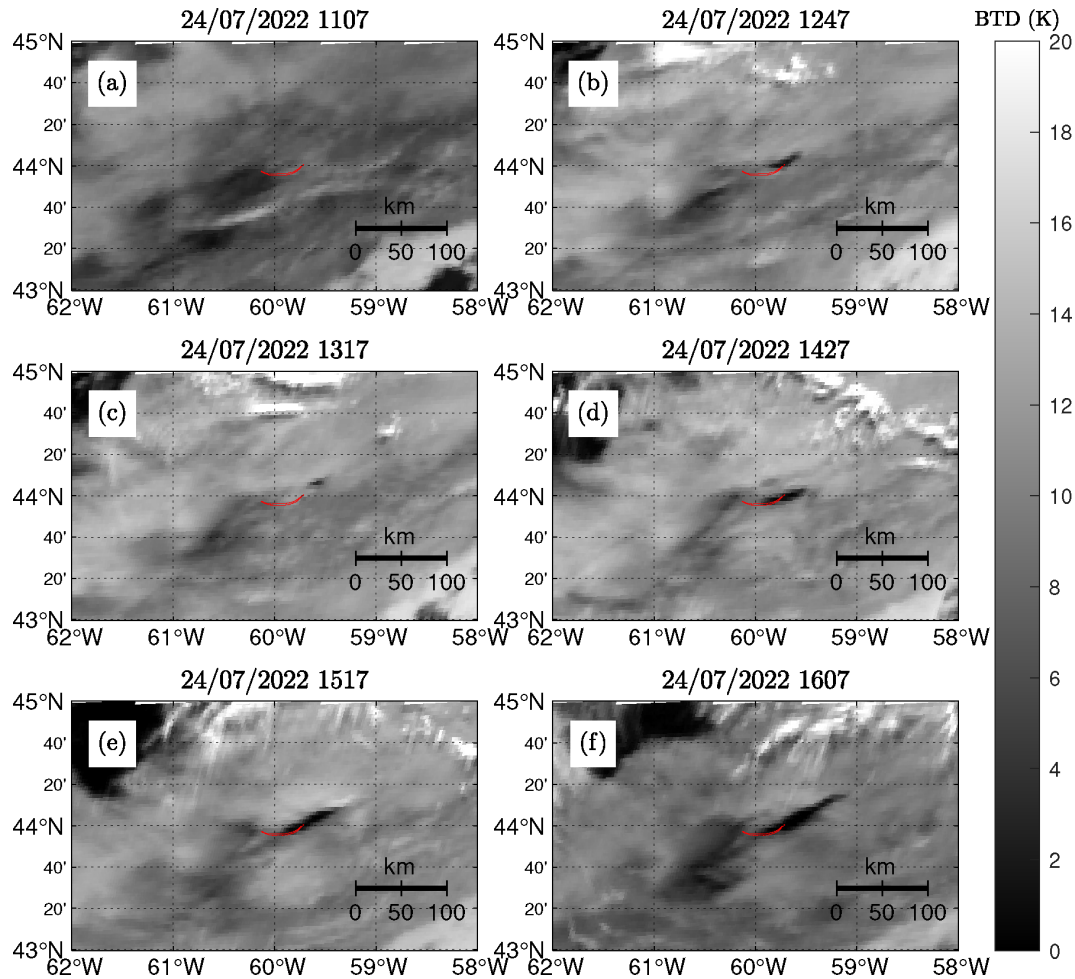


FIGURE 7 Brightness-temperature difference fields (10.35–3.9 μm) in the vicinity of Sable Island during July 24, 2022, as recorded by the *GOES-18* satellite. The individual panels were recorded at (a) 1107, (b) 1247, (c) 1317, (d) 1427, (e) 1517, and (f) 1607 ADT. [Colour figure can be viewed at [wileyonlinelibrary.com](https://onlinelibrary.wiley.com/doi/10.1002/qj.4891)]

and 2-m wind speed on SI are approximately constant at $5 \text{ m} \cdot \text{s}^{-1}$, with some decrease later. On SI, z_0 was estimated for all three tower locations using Equation (9) and the time-averaged U , u_* , and z/L during 1200–1800 ADT. The averaged z_0 values at the south ($z_0 = 0.013 \text{ m}$) and centre ($z_0 = 0.010 \text{ m}$) towers were quite close, but that at the north tower was smaller ($z_0 = 0.004 \text{ m}$), perhaps due to different surface conditions at the north tower compared with those at the other two towers. Nevertheless, the retrieved values are in reasonable agreement with the land classification of Davenport *et al.* (2000), who estimated $z_0 = 0.005 \text{ m}$ for bare soil and $z_0 = 0.03 \text{ m}$ for grassland. The ocean surface was relatively smooth, with on average $z_0 \approx 4 \times 10^{-5} \text{ m}$. The surface roughness over the ocean did not change much throughout the day, possibly due to constant winds. The rougher surface conditions on SI led to an enhanced friction velocity and higher turbulence levels (Figure 8b,e), but the approximate constancy of root-mean-square (RMS) velocity fluctuation suggests

an insubstantial contribution of convective turbulence at the tower measurement height of 2 m, which is addressed below.

There were stark differences in surface thermal conditions between SI and the upstream area. The SST was constant at 16°C during the fog shadow, with the 1-m ocean air temperature never exceeding the SST by more than 1°C (Figure 8d). The stability parameter (Figure 8f) over the ocean was near-zero for the entire day, indicating neutral conditions. The presence of a neutral stratification in the upstream area is advantageous for model–observation comparisons, since most of the theoretical IBL formulae of Table 1 assume neutral conditions. Conditions on SI were very different in that the 0–5 cm soil temperature reached temperatures up to 33°C during the afternoon, cooling down to about 19°C at night, all being higher than the SST upstream (16°C). Elevated soil temperatures allowed the air temperature to rise during the day, but, due to the short distance from the shore (e.g., $x \approx 370 \text{ m}$ at the centre

TABLE 3 Summary of IOP10.

Observations at SI	Time	Visibility
First appearance of fog	1845 ADT on July 23	100–300 m (all PWDs)
Disappearance of fog (start of fog shadow)	1030 ADT on July 24 (1200 ADT on July 24)	1–2 km at 2 m AGL, < 1 km at 8 m AGL
Reappearance of fog (end of fog shadow)	1800 ADT on July 24 (not visible from BTD)	100–200 m and steadily increasing on July 25
Final disappearance of fog	1800 ADT on July 25	2.5–5 km (all PWDs)

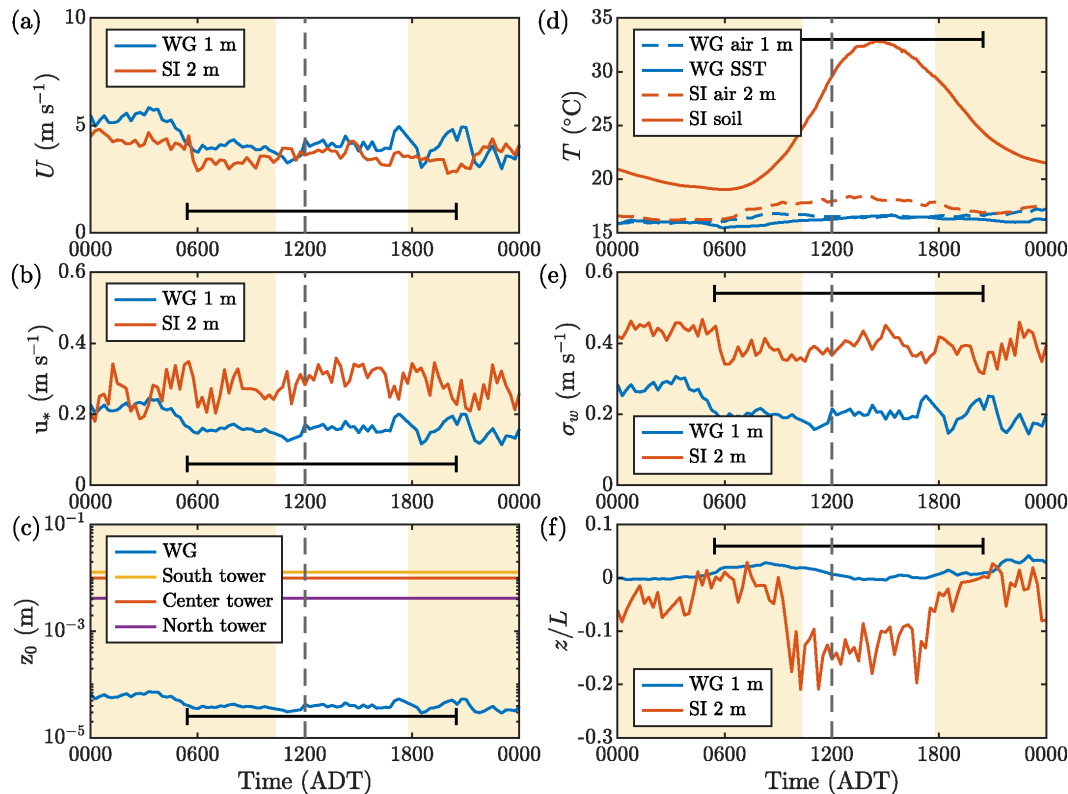


FIGURE 8 Time series of (a) near-surface wind speed, (b) friction velocity, (c) (momentum) surface-roughness length, (d) temperature, (e) vertical velocity fluctuations, and (f) stability parameter for July 24, 2022. The shaded areas denote foggy conditions. The dashed lines indicate the initial appearance of the fog shadow. Sunrise and sunset occurred at 0525 ADT and 2028 ADT, respectively, which is indicated by the black horizontal line. The measurements over the ocean were conducted at 1 m AGL on a Wave Glider (WG). The wind and temperature measurements on land are from 2 m AGL on the centre tower. [Colour figure can be viewed at [wileyonlinelibrary.com](https://onlinelibrary.wiley.com/terms-and-conditions)]

tower) and limited time of advection (about 1 min from the southern shore to the centre tower), the 2-m air temperature on SI only reached a maximum of 18.5°C compared with 16°C at night. During the night, H and ζ were approximately zero on SI, indicating neutral conditions, similar to the upstream ocean. During the day, the magnitude of the sensible heat flux increased to about 180 W · m⁻² and the stability parameter decreased to about -0.15, signifying unstable conditions during the day.

Figure 9 provides surface-layer energetics, including radiative fluxes (downwelling, upwelling, and net at 2 m) and a surface energy budget (SEB). Here, fluxes are defined positive when energy is carried towards the surface and negative when energy is carried away

from the surface. On a typical clear campaign day, the maximum downwelling shortwave radiative flux (SW_{\downarrow}) reached 1000 W · m⁻² (not shown), but during IOP10 it was reduced to 850 W · m⁻² as a result of a 100-m thick fog/mist layer (Figure 5e). On average, about 20% of SW_{\downarrow} was reflected by the surface as upwelling shortwave radiation SW_{\uparrow} during the day. The downwelling (LW_{\downarrow}) and upwelling (LW_{\uparrow}) longwave radiative fluxes were approximately equal in the morning and evening, due to the strong absorption of LW radiation within the fog layer. The fog layer “shielded” the warmer ground surface, and therefore the pyrgeometers recorded LW radiation originating predominantly from the fog droplets. Assuming an emissivity $\varepsilon = 1$, the Stefan–Boltzmann

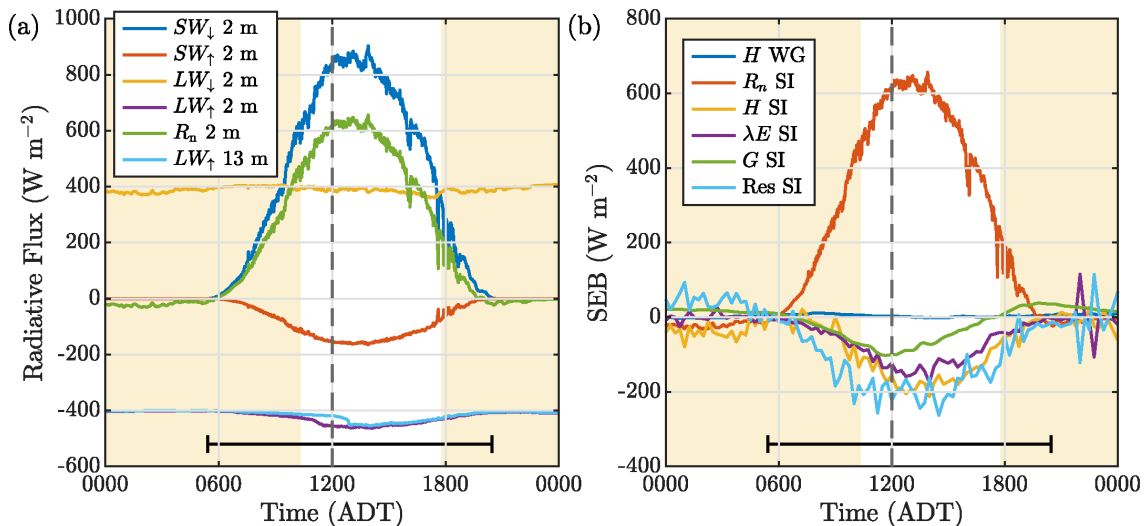


FIGURE 9 Time series of (a) radiative fluxes and (b) a surface energy budget for July 24, 2022. The radiative fluxes in (a) include upwelling and downwelling shortwave (SW_{\uparrow} , SW_{\downarrow}) and longwave radiative fluxes (LW_{\uparrow} , LW_{\downarrow}). Fluxes towards the surface are defined positive and fluxes away from the surface are defined negative. The surface energy budget in (b) includes the net radiation $R_n = SW_{\downarrow} + SW_{\uparrow} + LW_{\downarrow} + LW_{\uparrow}$, sensible heat flux H , latent heat flux λE , ground heat flux G , and residual term. The shaded areas denote foggy conditions. The dashed lines indicate the initial appearance of the fog shadow. [Colour figure can be viewed at [wileyonlinelibrary.com](https://onlinelibrary.wiley.com)]

law predicts a radiative temperature $T = (LW/\sigma)^{1/4} = (400/5.67 \times 10^{-8})^{1/4} \approx 16.7^\circ\text{C}$, which agrees well with the 2-m air temperature recorded by the T/RH probe. During the afternoon, when the fog shadow was present, the magnitude of the 2-m upwelling LW radiation increased slightly compared with the 2-m downwelling LW radiation, which remained constant. At 1200 ADT, the radiative temperature for upwelling LW radiation at 2 m AGL reached $T = (460/5.67 \times 10^{-8})^{1/4} \approx 27.0^\circ\text{C}$, which is much higher than the observed 2-m air temperature during this time but closer to the soil temperature. Owing to a reduction of the droplet number concentration and MVD close to the surface (Figure 5b,c), the absorption of LW radiation decreased and a downward-pointing pyrgeometer was now able to see the warmer ground surface ($T \approx 32^\circ\text{C}$). Note that a similar effect was observed for the 13-m upwelling LW radiation, but delayed by 1.5 hours. This reaffirms that visibility improvement (i.e., fog shadow) was generated at the surface of SI. The net radiation $R_n = SW_{\downarrow} + SW_{\uparrow} + LW_{\downarrow} + LW_{\uparrow}$ peaked at $600 \text{ W} \cdot \text{m}^{-2}$ during the period of the fog shadow.

Figure 9b shows the SEB for July 24, recorded near the centre tower. Typically, an SEB aims to quantify how the net radiation (R_n) is balanced by the sensible (H), latent (λE), and ground heat flux (G) in the absence of other energy sources and sinks. Many studies (Foken & Oncley, 1995; Mauder *et al.*, 2020) have shown that SEBs are difficult to close at time-scales less than several hours (e.g., over half-hour or, used in this study, 15-min averaging periods). On land, the sum $H + \lambda E + G$ is typically 20%–30% lower than the net radiation. This discrepancy

(or residual Res) arises because the fluxes are measured not exactly at the land–atmosphere interface, but slightly above and below it (e.g., turbulence measurements at 2 m AGL), leading to undesirable storage and advection terms. Due to this observed imbalance, the SEB is usually formulated as

$$R_n + H + \lambda E + G + Res = 0. \quad (14)$$

Here, fluxes are defined as positive when energy is carried towards the surface and negative when energy is carried away from the surface. During the night, R_n was slightly negative, but at 0600 ADT it increased and followed a typical diurnal cycle of radiation. At the same time, the magnitude of the sensible and latent heat flux increased to $200 \text{ W} \cdot \text{m}^{-2}$. The ground heat flux reached a peak value of $100 \text{ W} \cdot \text{m}^{-2}$ at 1200 ADT and decreased afterwards. The residual term accounts for roughly 30% of the net incoming radiation, which is comparable with the aforementioned studies. Grachev *et al.* (2020) showed that, for wet and dry soils, the residual term can be significantly reduced using daily or longer averaging. Note that, in our case, it was not feasible to use averaging times of several hours due to the rapid fog formation and dissipation.

The fog and IBL observations in Figures 4–9 can be summarized as follows.

1. The wind speed, wind direction, temperature, RH, and TKE during IOP10 (Figure 4) for the centre tower suggest that the change of visibility conditions on SI and in its “shadow” is due to changes of local conditions,

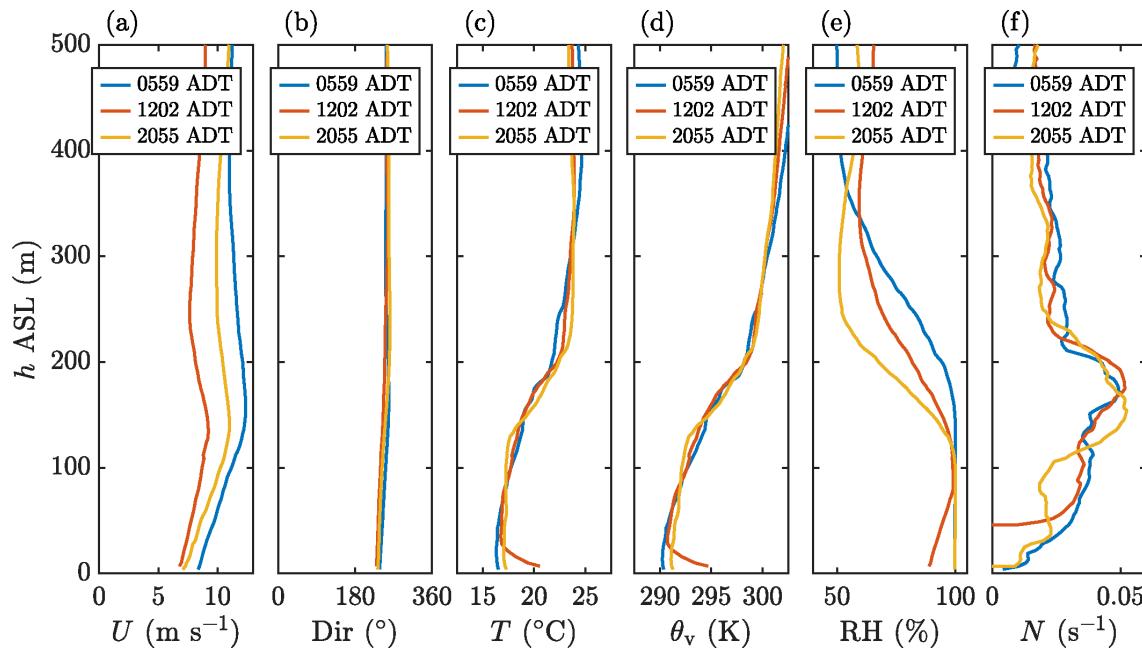


FIGURE 10 Vertical profiles of (a) wind speed, (b) wind direction, (c) temperature, (d) virtual potential temperature, (e) relative humidity, and (f) Brunt-Väisälä frequency as measured by a radiosonde. The radiosondes were released on July 24, 2022 at 0559, 1202, and 2055 ADT near the centre tower. [Colour figure can be viewed at [wileyonlinelibrary.com](https://onlinelibrary.wiley.com/doi/10.1002/qj.4891)]

since the wind speed and direction (Figure 4a,b) and upstream RH (Wave Glider, Figure 4d) do not change appreciably during the observational period.

- There was a significant increase of temperature (and reduction of RH) on SI during the low-level fog dissipation period, highlighting the role of a thin air layer near the surface. Near-surface data in Figure 8 at 2 m height on the centre tower and the area upwind of SI show approximately similar mean velocities, but an enhancement of the friction velocity (Figure 8b), roughness length (Figure 8c), and RMS vertical velocity fluctuations (Figure 8e) over SI suggested the development of an IBL over land. The constancy of RMS vertical velocity fluctuations and friction velocities over SI during the fog dissipation period and the concomitant rapid rise of temperature over land suggest that a reduction of RH due to temperature rise is the cause of near-surface fog dissipation.
- The energy fluxes over SI (Figure 9b) show a net radiative flux of $500 \text{ W} \cdot \text{m}^{-2}$ to the surface layer (at 2 m). The MOST stability parameter (Figure 8f) shows unstable conditions over SI during fog dissipation but near-neutral or slightly stable conditions over the ocean. The diabatic heating near the ground due to net radiation influx within a layer of 25 m is evident from the radiosonde profiles shown in Figure 10. At 0600 ADT on July 24, just after sunrise, the air temperature increases from 16°C to 17°C at the higher levels and to 18°C at the lower levels (Figure 4c),

forming a superadiabatic layer close to the surface. The relative humidity also dropped, starting at 1130 ADT (Figure 4d). The heating and drying continued throughout the day, peaking around 1400 ADT, after which the air temperature started decreasing and the RH increasing. Again, air reached saturation at 1800 ADT, leading to the reappearance of fog (Figure 4). A summary of these observations is given in Table 3.

- The dominance of shear-generated mechanical turbulence ($-\overline{u'w'}\partial U/\partial z$) over contributions of thermally generated convective turbulence ($(g/\theta_v)\overline{\theta'_v w'}$) was clearly evident from the data. Their relative contributions are signified by the flux Richardson number Ri_f , defined as

$$Ri_f = -\frac{\frac{g}{\theta_v}\overline{\theta'_v w'}}{\overline{u'w'}\frac{\partial U}{\partial z}}, \quad (15)$$

which is related to the Monin-Obukhov similarity function as $Ri_f \approx z/L$ (Kaimal & Finnigan, 1994). Note that in Figure 8f, during the entire measurement period, $|Ri_f| = |z/L| \leq 0.15$, which clearly indicates that buoyant production is unimportant compared with shear production, and hence TKE is dependent only on the latter. Since the velocity U remains constant before 0600 UTC on July 25, the TKE remained constant irrespective of any changes in the buoyancy forcing. After this time, U increases and hence TKE increases, but this period is outside the window of interest of our analysis.

In addition, it is possible to evaluate convective and mechanical contributions to the TKE. The characteristic RMS vertical velocity fluctuation σ_w prior to fog dissipation is $0.4 \text{ m} \cdot \text{s}^{-1}$ (Figure 8e). Since the convective velocity contribution during the fog dissipation period is around $\alpha w_* = 0.5(q_0 h)^{1/3} \approx 0.2 \text{ m} \cdot \text{s}^{-1}$, where $h \approx 25 \text{ m}$ is the convective-layer thickness, q_0 is the buoyancy flux, and $\alpha \approx 0.5$ at measurement height $z/h \approx 0.08$, it appears that the convective contribution is weak $((\alpha w_*/\sigma_w)^3 \approx 0.2)$, Equation 2). This clearly shows why TKE remains constant as far as U remains constant, although the heat flux varies during the diurnal cycle. Note that, further downstream, convective turbulence could become more important as the IBL height h and therefore w_* continues to grow.

- The Wave Glider recorded a relative humidity of 100% for the entire duration of the fog shadow (Figure 4d, solid line), as its RH sensor was located close to the ocean surface (1 m). Nevertheless, these measurements agree with the notion of local reduction of RH on SI, confirming that daytime heating and drying over SI led to improved visibilities on SI and in the area downstream (i.e., the fog shadow).

5.2 | Radiosonde and TBS observations

The significant differences of roughness (Figure 8c) and surface temperatures (Figure 8d) observed between the ocean and SI point to conditions conducive for momentum and thermal IBLs originating at the southern coast of SI on July 24. Radiosonde and TBS profiles, obtained in the vicinity of the centre tower (Figure 2d) provide insights into these IBLs, which are described below. Figure 10 shows vertical profiles of wind speed and direction, T , θ_v , RH, and the Brunt-Väisälä frequency $N = \sqrt{(g/\theta_v)\partial\theta_v/\partial z}$ as recorded by radiosondes launched from SI before (0559 ADT), during (1202 ADT), and after (2055 ADT) the appearance of the fog shadow. Prior to calculating N , the profiles of θ_v were smoothed with a window of 40 m. The variability of wind direction and speed are minor (see also Figures 4a,b and 8a), likely due to perturbations of environmental conditions. The θ_v and N profiles (Figure 10d,f) show a stable stratification at higher elevations, which becomes weaker above 200 m ASL. Before the appearance of the fog shadow at 1100 ADT, the stratification in the bottom 50 m was near-neutral (Figure 8f), consistent with low sensible heat flux on SI and a small heat flux over the ocean, and the lower 110 m had a relative humidity of 100%, consistent with a 100-m thick fog layer (Figure 5e).

Figure 11 shows profiles of T , RH, and the gradient Richardson number Ri from 1300–1900 ADT recorded by the tethered balloon system, which reached an altitude of

100 m AGL. Ri was calculated as

$$Ri = \frac{N^2}{\left(\frac{\partial U}{\partial z}\right)^2}, \quad (16)$$

and was smoothed over a window with a height of 30 m. The first profile was taken at 1316 ADT, just before the end of the first fog shadow (Figure 7b,c). It shows a shallow superadiabatic layer that extends up to 25 m AGL, similar to profiles taken an hour earlier (Figure 10). Ri profiles (Figure 11c) displayed an unstable ($Ri < Ri_c = 0.25$) layer at 0–30 m, which is similar to the depth of the superadiabatic layer (25 m AGL). Pronounced vertical variability of T was evident in the superadiabatic layer, possibly contributed to by ground-distorted eddies of convective turbulence (originating from the unstable temperature gradient). The relative humidity close to the ground was about 90% and reached saturation at 100 m above the ground. Curiously, at 1354 ADT, there was a slight reduction of the air temperature close to the ground. The relative humidity increased to 100%, which is possibly related to a temporary vanishing of the fog shadow observed by satellite observations (Figure 7c). There is no indication that this reduction of T and increase of RH were a local phenomenon, since the opposite was expected with increasing local ground heat flux (Figure 9b). The temperature at this time over the column at height 20–60 m AGL was reduced by half a degree or so, which persisted until 1730 ADT. This reduction of T at 1354 ADT was associated with an increase of RH to 100% momentarily, which relaxed to an unsaturated state by 1456 ADT. Thus, the increase in RH, and possibly related disruption of the fog shadow, was evident only for a short period from 1315–1415 ADT. It is possible that a short-lived mixing event brought down air from a saturated or near-saturated layer that was consistently present at heights 60–125 m, as hinted by the gradient Richardson number (Figure 11c), which showed the temporary growth of the unstable layer from 30 m to 50 m AGL. Alternatively, the increase in RH may have been due to a change in the upstream conditions that was simply advected over SI. The final vertical profile at 1832 ADT shows reduced temperature and saturated air close to the ground during the evening transition (Figure 8d), which indicates that by this time the fog shadow is starting to disappear (e.g., similar to Figure 7c).

5.3 | Internal boundary-layer height

Motivated by the inference that the fog shadow appeared in conjunction with a thermal IBL over a warm surface, a study on the IBL development over SI was conducted. Figure 6a–c clearly demonstrates that the fog-free layer

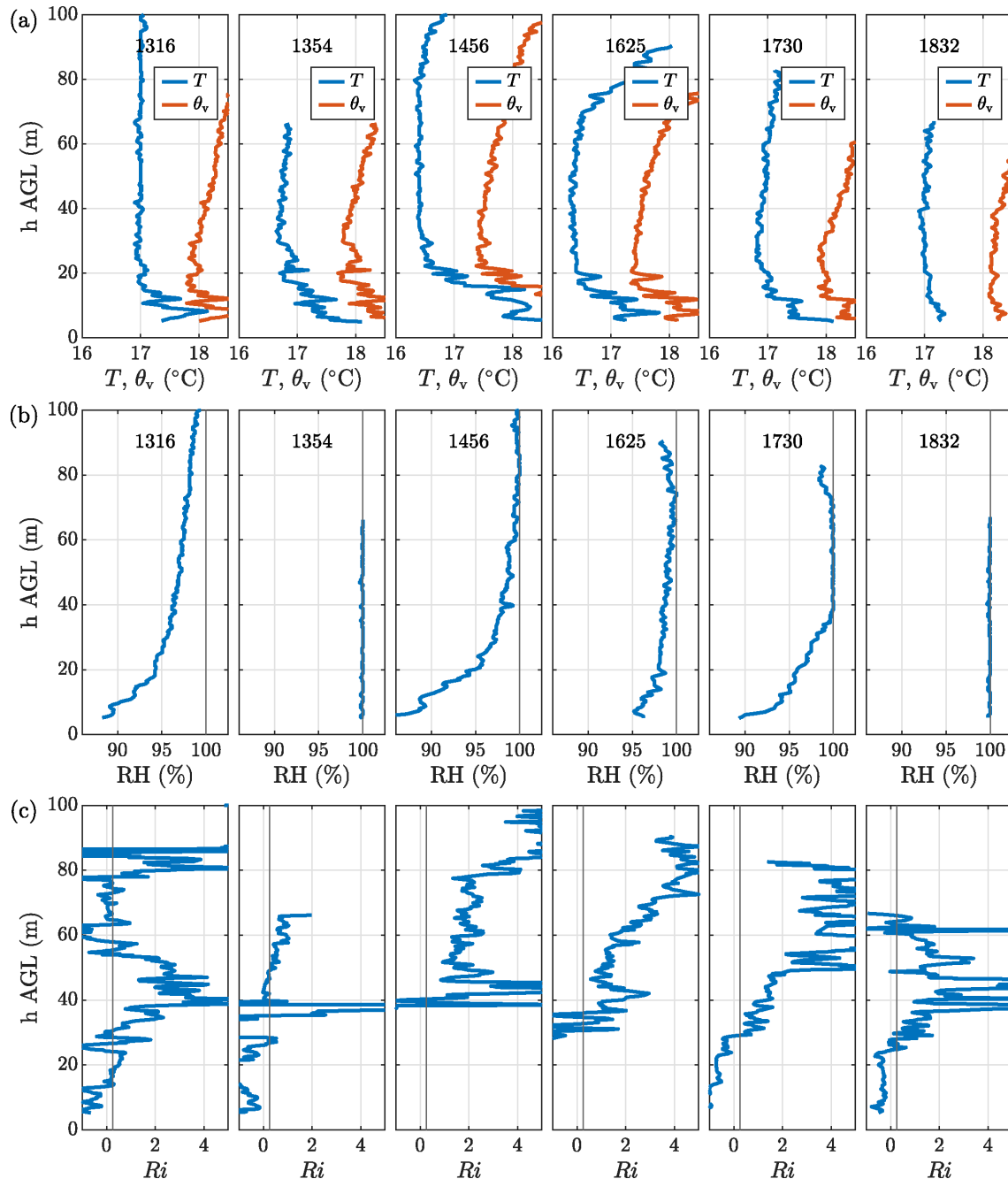


FIGURE 11 Several (a) temperature, (b) relative humidity, and (c) gradient Richardson number profiles on Sable Island on July 24, 2022 from 1316–1848 ADT, recorded by the TBS. The first fog shadow was present in the profiles recorded at 1316 ADT. Fog is observed close to the surface in the 1354 ADT profile. The second fog shadow is visible in the 1456, 1625, and 1730 ADT profiles. The second fog shadow has likely disappeared by 1832 ADT. [Colour figure can be viewed at [wileyonlinelibrary.com](https://onlinelibrary.wiley.com/doi/10.1002/qj.4891)]

develops with distance from the southern shore and time. At the south tower, no fog-free layer was observed within the resolution of the CL31, but the visibility increase registered by the PWD at 2 m and the temperature profiles indicate a thin IBL (Figure 6e). At the centre and north towers, the fog-free layer becomes 25 and 30 m thick. Air from this warmer IBL is advected over the ocean past the north tower, causing the fog shadow.

Several methods have been used to quantify the IBL height, as reviewed by Savelyev and Taylor (2005). The most convenient is perhaps the use of mean wind-speed profiles taken upstream and downstream of the discontinuity, and locating the height at which they converge; this is untenable in our case, since profiles are available only for downstream locations. Another method is to locate $\partial U/\partial z$ discontinuities or wind-speed

“kinks” in individual velocity profiles (Antonia & Luxton, 1971, 1972; Elliott, 1958; Garratt, 1990; Panofsky & Townsend, 1964), recognizing that velocity profiles above and below the kink are governed by upstream and downstream surface-roughness lengths, respectively. Alternatively, Shir (1972) determined the IBL height using stresses. If discontinuities of the surface temperature or heat flux are present (e.g., Figure 8), then a thermal IBL develops, and kinks in virtual potential temperature ($\partial\theta_v/\partial z$) profiles downstream of the discontinuity can be used to identify the height of the thermal IBL. The influence of the upstream and downstream surfaces in this case can be observed through the distinct slopes (lapse rates) above and below the kink, respectively.

In the radiosonde profiles of U at SI shown in Figure 10a, a kink of U could be observed only at a height of 200 m ASL, but this height is deemed unrealistic to be the top of the IBL developing on SI. The distance between the locations of the ocean–land discontinuity and radiosonde launch (or fetch) is 400 m; as discussed later, rough calculations of the IBL height h using almost all available formulae (Table 1) show that h cannot exceed ~ 50 m. There is no evidence for a kink in the profile closer to the surface, which is consistent with the observations shown in Figure 8a that illustrate no significant systematic reduction of U over SI at 2-m height compared with the ocean upstream. Thus U at heights viable for radiosonde profiling has not yet responded to increased surface roughness over SI, although the friction velocity did respond to increased roughness, with an increase from 0.2 to 0.3 $\text{m} \cdot \text{s}^{-1}$. Such behaviour has also been noted in the numerical studies of Shir (1972).

On the other hand, the θ_v profiles in Figure 10 show two kinks, the first at 200 m ASL, similar to the velocity profile, and a second one at 31 m ASL only at 1202 ADT. As mentioned, the kink at 200 m ASL cannot be the IBL height, but possibly represents the height of the background marine atmospheric boundary layer (MABL), h_{MABL} . This notion is consistent with the MABL height evaluated using the Zilitinkevich *et al.* (2012, fig. 2) expression $h_{\text{MABL}} = 0.15(u_*/f) \approx 225$ m, where $u_* \approx 0.15 \text{ m} \cdot \text{s}^{-1}$ and the planetary vorticity $f \approx 1.0 \times 10^{-4} \text{ s}^{-1}$. The second kink may in fact correspond to the (thermal) IBL height, separating the superadiabatic near-surface layer over the land surface of SI from a near-neutral or slightly stable lapse rate over the ocean. The TBS profiles in Figure 11 also exhibit similar kinks in the temperature profiles, as evident from Figure 12, where interpolated time–height cross-sections of θ_v and RH based on the TBS profiles are shown. Also shown are the height estimates of the thermal IBL determined by the kinks of individual θ_v profiles. The locations of the kinks were determined by finding the height at which $\partial\theta_v/\partial z = 0$ for each individual profile, since a neutral stratification was present in the absence of heating before and after the fog shadow ($H \approx 0$, see Figure 9b). The estimated IBL height was approximately constant with time, with an average of $h = 25 \pm 5$ m AGL. This is consistent with the notion that the thermal IBL height is determined by vertical diffusion of T from heating of the SI surface in the backdrop of approximately stationary turbulence over SI (Figure 8b,e).

Based on Figures 8 and 12, the period between 1200 and 1800 ADT was identified, during which several key parameters (e.g., wind speed, wind direction, heat flux)

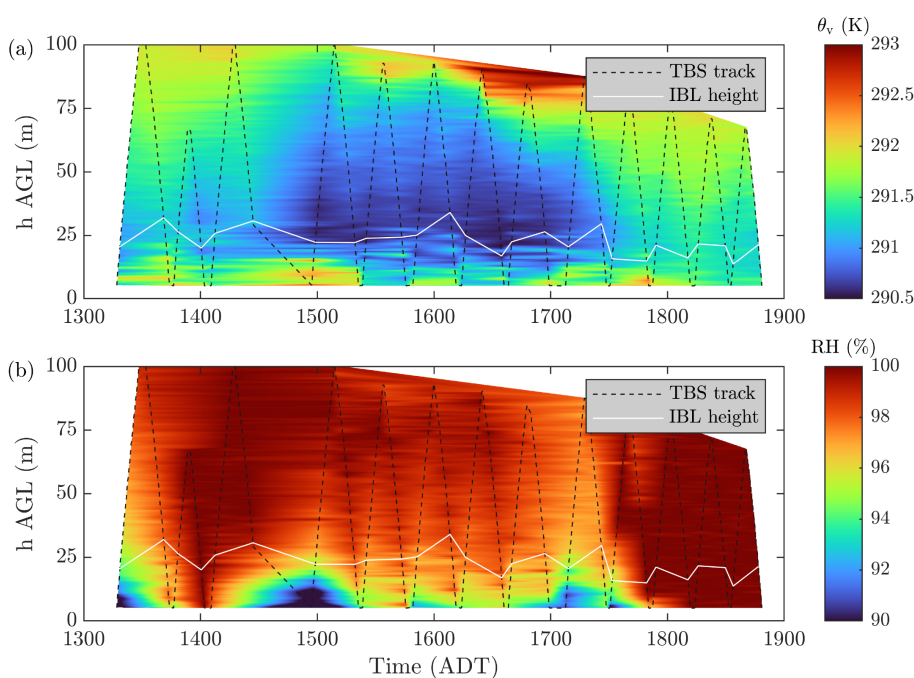


FIGURE 12 Time-height cross-sections of (a) virtual potential temperature and (b) relative humidity based on interpolated TBS profiles on Sable Island on July 24, 2022 from 1316–1848 ADT. The dashed lines indicate the time and height of the tethered balloon at a given instant. The white line shows the IBL height based on virtual potential temperature measurements of individual profiles. [Colour figure can be viewed at wileyonlinelibrary.com]

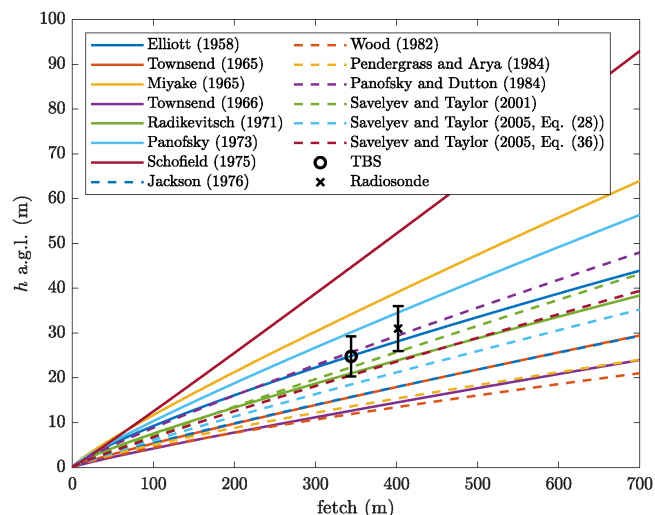


FIGURE 13 Comparison of the observed IBL height on Sable Island with the theoretical expressions in Table 1. The observed IBL height reflects the average IBL height of individual profiles recorded during 1200 – 1800 ADT. [Colour figure can be viewed at wileyonlinelibrary.com]

and the IBL height were approximately constant. This period can be used for comparison with theoretical expressions derived for steady-state IBLs. Figure 13 shows a comparison of the thermal IBL height h estimated from radiosonde and TBS measurements and theoretical expressions listed in Table 1 for this steady-state period. Note that the formulae in Table 1 often assume similar diffusion of momentum and heat (as a passive scalar) by turbulent fluctuations, allowing the use of thermal IBL height for comparisons. In fact, complex dynamical adjustments of shear stresses at the discontinuity make temperature the most appropriate marker for comparison with IBL formulae (see below).

The IBL height h estimated from TBS profiles of θ_v was 25 ± 5 m AGL for a fetch ≈ 350 m. The radiosonde measurements showed $h \approx 33 \pm 5$ m ASL or 31 ± 5 m AGL at a fetch ≈ 400 m. The expressions for h in Table 1 were evaluated using the following parameters taken from Figure 8: upstream (ocean) surface roughness $z_{0U} = 4 \times 10^{-5}$ m, downstream (SI centre tower) surface roughness $z_{0D} = 0.01$ m, $L_U \approx 2.3 \times 10^3$ m, and $L_D \approx 13.3$ m. Overall, the variability of h predictions based on Table 1 is profound, and naturally the two measured IBL heights in Figure 13 are insufficient to draw sound conclusions on the accuracy of a specific formula. Rather, it shows that these different approaches lead to a range of IBL heights. In this case, the formulae of Elliott (1958) and Panofsky and Dutton (1984) agreed best with the data, with a difference of less than 5%. Many formulae underestimated h , a contributor to which may be the underlying assumption of neutral stratification. For example, the expression of

Saveliev & Taylor (2005, Eq. (36)) for a diabatic IBL height is somewhat larger than the equivalent expression (Saveliev & Taylor, 2005, Equation (28)) for neutral conditions.

A brief discussion is in order on the absence of IBL signatures in velocity profiles although the thermal IBL is identifiable. In the latter case, the heat generated at the SI surface is simply diffused upward by approaching (inhomogeneous but stationary) background turbulence, and the distribution of temperature downstream of the discontinuity is easily detectable during this process as the thermal IBL. On the other hand, the momentum (velocity profile) adjustment is more complex and dynamical, first occurring through a pressure rise at the discontinuity acting to smooth the velocity discontinuity (Onishi & Estoque, 1968), followed by an adjustment region of friction velocity (stresses) from upstream (u_{*U}) to downstream (u_{*D}) accompanied by enhanced turbulence production at the land surface. The downstream vertical diffusion length of the momentum deficit in this case can be parameterized as $d \sim (u_{*D} - u_{*U})x/U \approx (0.28 - 0.17)350/5 \approx 8$ m (Mulhearn, 1977; Townsend, 1976), which is not detectable accurately by radiosonde or TBS profiles. This inference is consistent with the laboratory observations of Antonia and Luxton (1971) that the velocity-profile adjustment is not completed until far downstream of the discontinuity.

6 | DISCUSSION

The observations presented in Sections 4 and 5 clearly established the formation of an IBL over SI on July 24, which was devoid of fog due to daytime heating of the ground and consequent reduction of the relative humidity. Near the centre tower, the height of the fog-free IBL was $h \approx 25$ m at a fetch of 350–400 m. The full fog layer was 100 m thick, hence fog was still present at 25–100 m AGL. The satellite observations presented in Figure 7 suggest that there was a region downstream of SI devoid of fog (i.e., fog shadow), where the entire 100-m thick fog layer had been dissipated (with $BTD \approx 0$). However, the presence of such a fog shadow could not be confirmed directly with in situ measurements, as the R/V *Atlantic Condor* was not located downwind of SI at that time.

The fact that the fog dissipation on SI occurred in an IBL suggests that the wind fetch over SI is important, since it determines the maximum IBL height that can be reached over SI. The maximum fetch is sensitive to the wind direction and longitude, as can be seen from Figure 2a. The SI measurement site was located on the western side of the island, where the maximum fetch is 700 m. Longer fetches can be reached on the centre and eastern part of SI; for example, at SI's widest point (1.2 km wide), the full fetch given west–southwesterly winds is 3 km. If we were to

take the two best-performing IBL formulae (Elliott, 1958; Panofsky & Dutton, 1984) and calculate their IBL heights for larger fetches, we find that the IBL height surpasses 100 m at $x \approx 1.5\text{--}2.0$ km, which suggests that dissipation of the full fog layer is possible on SI. However, it should be noted that it is not guaranteed that the Elliott (1958) and Panofsky and Dutton (1984) expressions are also accurate at larger fetches. Additionally, this analysis ignores the fact that there is a stable stratification present at 50–200 m AGL, which may dampen the IBL growth in this range.

It is remarkable that the fog shadow was able to extend to 80 km downstream of SI, even though SI is only 1.2 km wide. In this downstream region, where a rough-to-smooth IBL is present, fog was slowly recovered, but unfortunately this region could not be studied due to the lack of direct measurements downstream of SI. A plausible explanation for such an elongated fog shadow is as follows. On SI, the sensible heat flux was relatively high and upward ($175\text{--}200 \text{ W} \cdot \text{m}^{-2}$) due to the large temperature difference between the surface soil (up to 32°C) and approaching air from the upstream MABL ($\sim 16^\circ\text{C}$). Downstream of SI, however, the air temperature is a few degrees higher than the SST (i.e., the heat flux reverses), which helps cool downstream air to eventually form fog. This flux reversal is slower, given the time needed for all turbulent eddies (from the integral ℓ down to the Kolmogorov scales) to feel the new thermal condition. According to Fernando and Hunt (1996), this time is $4\tau_e$, where $\tau_e \approx \ell/\sigma$ is the large eddy turnover time-scale. Taking [the measured] $\ell \approx 100$ m and the RMS velocity $\sigma \approx u_* \approx 0.5 \text{ m} \cdot \text{s}^{-1}$, the downstream length where the ocean cooling is first felt can be estimated as $4U\tau_e \approx 4$ km. [There were ship-based measurements in the fog shadow area during July 26–27, 2022 (IOP11), but unfortunately the fog shadow was absent on that day; the above ℓ and u_* were based on these measurements, where $U \approx 5 \text{ m} \cdot \text{s}^{-1}$ (Ortiz-Suslow *et al.*, 2024).] The length required for effective cooling downstream of the island is expected to be much larger than $4U\tau_e$ (e.g., see Townsend, 1976, p. 298), considering other factors necessary for fog, such as a larger drop of temperature needed to reach the dew point and aerosol availability.

This study is part of the FATIMA project, which aims to study the interaction between fog and turbulence in the marine atmosphere. The SI measurement site was selected due to its small size (minimum disturbances) and favourable location with high occurrence of marine fog (Dorman *et al.*, 2019). Notwithstanding its small size, the present study shows that IBLs are formed over SI and disturb fog advection over the island profoundly. For IOP10, increased daytime soil temperature at SI was a critical factor leading to fog dissipation, although other

factors such as increased surface roughness, convective turbulence, and lee-edge boundary layer may have played lesser roles. More studies are needed to delineate the relative roles of such influencers, and to this end various research groups are working with FATIMA–GB datasets on IBLs.

7 | CONCLUSION

Observations of a fog-free region (or fog shadow) over and downstream of an islet when a fog-laden marine atmospheric boundary layer advected past the islet were described in this article. The measurements were made during IOP10 of the FATIMA field campaign in the Northern Atlantic on Sable Island (SI). The fog shadow phenomenon was predicted by the Naval Research Laboratory's COAMPS[®] mesoscale model that was used to guide the field campaign. The fog-free layer on SI, which likely led to a fog shadow downstream of SI, appeared at 1200 ADT, as identified by a visibility greater than 1 km, while the conditions upstream of SI remained foggy and saturated, which is evident from satellite images and measurements by an instrumented Wave Glider. The onset of the fog shadow followed intermittent periods of fluctuating visibility in the “mist” range (1–2 km). The fog shadow likely started disappearing for the day at 1800 ADT. Background environmental perturbations appear to be the cause of visibility fluctuations and intermittent appearance of fog in the fog shadow. Satellite observations showed that the fog shadow extended tens of kilometres downstream of SI over the ocean, before possibly returning to upstream conditions.

It was hypothesized that either the reduction of relative humidity (RH) during daytime ground heating, enhanced turbulence, or a combination thereof leads to the fog shadow. However, the wind speed and direction as well as RMS and frictional velocities on the ocean and land were approximately constant during the observational period, and hence enhanced turbulence as a cause of the fog shadow was discounted.

Surface energy budget measurements showed significant radiative heating on SI during the fog shadow. The surface heating on SI was pronounced, with a 15°C higher soil temperature than the SST of the surrounding ocean at midday. The momentum surface roughness of SI was estimated to be two orders of magnitude larger than that over ocean. As such, the development of velocity and thermal smooth-to-rough IBLs above the land were expected, thus confining warmer air temperature with reduced RH (devoid of fog) into a layer with the thickness of the IBL. The IBL was considered as the layer in which the temperature gradient was superadiabatic. The

sensible heat flux and stability parameter indicated neutral conditions over the ocean and unstable conditions on SI during the day, but the contribution of convective turbulence was insignificant because of the smaller thickness of the IBL and stronger shear-generated turbulence. For larger fetches, convective turbulence could be more important.

A cross-SI transect of three ceilometers illustrates the streamwise growth of an IBL, showing that the fog shadow is confined to a thin layer of thickness of 25 m at the centre of SI. The thickness of the thermal IBL was \sim 25 m, as evaluated by tethered balloon and radiosonde observations. Above this layer, the fog dissipation was negligible, further suggesting that the fog shadow is a surface-heating-dominated phenomenon confined to the IBL. The velocity IBL, however, was undetectable by these two vertical profiling platforms, since the velocity profiles adjusted much more slowly compared with the thermal IBL and therefore it was not possible to detect kinks in the velocity profiles related to the IBL on SI. Since most IBL models assume simple vertical diffusion of momentum and scalars by turbulence, they describe the thermal IBL growth more aptly, allowing a comparison with measurements. The differences of predictions by available IBL models were acute, and thus radiosonde/tethered-balloon observations made at two nearby locations were insufficient to make conclusions on the efficacy of the models, although several of the models predicted an accurate IBL height.

ACKNOWLEDGEMENTS

The authors thank Kelly Huang, Thomas Hintz, Jay Orson Hyde, Ronald Scott Coppersmith, Evan Newman, Eric Pardyjak, Alexei Perelet, Alexis Trottier-Paquet, Reno Sit, Ryan Yamaguchi, and Nick Pizzo for their contributions to the data collection on Sable Island and for the Wave Glider. Additional special thanks go to Paul Leblanc, Marvin Willis, Jason Surette, and the Parks Canada team for their logistical contributions to the Sable Island operations during FATIMA-GB.

CONFLICT OF INTEREST STATEMENT

The authors declare no conflict of interest.

DATA AVAILABILITY STATEMENT

Data are available on request from the authors.

ORCID

Stef L. Bardoel  <https://orcid.org/0009-0002-5563-285X>

Andrey A. Grachev  <https://orcid.org/0000-0002-7143-0820>

Saša Gaberšek  <https://orcid.org/0000-0002-2287-8776>

REFERENCES

- Adrian, R.J., Ferreira, R.T.D.S. & Boberg, T. (1986) Turbulent thermal convection in wide horizontal fluid layers. *Experiments in Fluids*, 4, 121–141.
- Amani, M., Mahdavi, S., Bullock, T. & Beale, S. (2020) Automatic nighttime sea fog detection using goes-16 imagery. *Atmospheric Research*, 238, 104712.
- Antonia, R.A. & Luxton, R.E. (1971) The response of a turbulent boundary layer to a step change in surface roughness part 1. Smooth to rough. *Journal of Fluid Mechanics*, 48, 721–761.
- Antonia, R.A. & Luxton, R.E. (1972) The response of a turbulent boundary layer to a step change in surface roughness. Part 2. Rough-to-smooth. *Journal of Fluid Mechanics*, 53, 737–757.
- Bardoel, S.L., Horna Muñoz, D.V., Grachev, A.A., Krishnamurthy, R., Chamorro, L.P. & Fernando, H.J.S. (2021) Fog formation related to gravity currents interacting with coastal topography. *Boundary-Layer Meteorology*, 181, 499–521.
- Charnock, H. (1955) Wind stress on a water surface. *Quarterly Journal of the Royal Meteorological Society*, 81, 639–640.
- Coccal, O. & Belcher, S.E. (2004) A canopy model of mean winds through urban areas. *Quarterly Journal of the Royal Meteorological Society*, 130, 1349–1372.
- Colville, D., Reeves, B., Ure, D., Livingstone, B. & Stewart, H. (2016) Mapping the topography and land cover of Sable Island. *Proceedings of the Nova Scotian Institute of Science*, 48, 285–307.
- Davenport, A.G., Grimmond, C.S.B., Oke, T.R. & Wieringa, J. (2000) Estimating the roughness of cities and sheltered country. In: *Preprints, 12th Conf. On applied climatology*, Vol. 96, p. 99. Asheville, NC: Amer. Meteor. Soc.
- Deardorff, J.W. (1983) A multi-limit mixed-layer entrainment formulation. *Journal of Physical Oceanography*, 13, 988–1002.
- Dorman, C.E., Mejia, J., Koračin, D. & McEvoy, D. (2019) World marine fog analysis based on 58-years of ship observations. *International Journal of Climatology*, 40, 145–168.
- Elliott, W.P. (1958) The growth of the atmospheric internal boundary layer. *Transactions, American Geophysical Union*, 39, 1048–1054.
- Fernando, H.J.S., Dorman, C.E., Pardyjak, E., Shen, L., Wang, Q., Creegan, E. et al. (2024) Fatima-GB: searching clarity within marine fog. *Bulletin of the American Meteorological Society*.
- Fernando, H.J.S., Gultepe, I., Dorman, C., Pardyjak, E., Wang, Q., Hoch, S.W. et al. (2021) C-fog: life of coastal fog. *Bulletin of the American Meteorological Society*, 102, E244–E272.
- Fernando, H.J.S. & Hunt, J.C.R. (1996) Some aspects of turbulence and mixing in stably stratified layers. *Dynamics of Atmospheres and Oceans*, 23, 35–62.
- Fernando, H.J.S., Wang, S., Huang, K.Y. & Creegan, E. (2023) Fog-laden density staircases in the marine atmospheric boundary layer. *Environmental Fluid Mechanics*, 23, 489–510.
- Foken, T. & Oncley, S. (1995) Workshop on instrumental and methodical problems of land surface flux measurements. *Bulletin of the American Meteorological Society*, 76, 1191–1193.
- Gaberšek, S., Gapp, N., Bardoel, S. L., Fernando, H. J. S., Ruiz-Plancarte, J., Ortiz-Suslow, D. G., Wang, Q., Pardyjak, E., Hoch, S., Gultepe, I. & Dorman, C. (2024) Fog clearing in the lee of an isolated flat Island: a fog shadow. *Q J R Meteorol Soc.* (submitted).
- Gao, S., Lin, H., Shen, B. & Fu, G. (2007) A heavy sea fog event over the yellow sea in march 2005: analysis and numerical modeling. *Advances in Atmospheric Sciences*, 24, 65–81.

- Garratt, J.R. (1990) The internal boundary layer—a review. *Boundary-Layer Meteorology*, 50, 171–203.
- Gautam, R. & Singh, M.K. (2018) Urban heat Island over delhi punches holes in widespread fog in the indo-gangetic plains. *Geophysical Research Letters*, 45, 1114–1121.
- Grachev, A.A., Fairall, C.W., Blomquist, B.W., Fernando, H.J.S., Leo, L.S., Otárola-Bustos, S.F. et al. (2020) On the surface energy balance closure at different temporal scales. *Agricultural and Forest Meteorology*, 281, 107823.
- Grachev, A.A., Krishnamurthy, R., Fernando, H.J.S., Fairall, C.W., Bardoel, S.L. & Wang, S. (2021) Atmospheric turbulence measurements at a coastal zone with and without fog. *Boundary-Layer Meteorology*, 181, 395–422.
- Grachev, A.A., Leo, L.S., Fernando, H.J.S., Fairall, C.W., Creegan, E., Blomquist, B.W. et al. (2018) Air–sea/land interaction in the coastal zone. *Boundary-Layer Meteorology*, 167, 181–210.
- Grare, L., Statom, N.M., Pizzo, N. & Lenain, L. (2021) Instrumented wave gliders for air–sea interaction and upper ocean research. *Frontiers in Marine Science*, 8, 664728.
- Gultepe, I., Agelin-Chaab, M., Komar, J., Elfstrom, G., Boudala, F. & Zhou, B. (2019) A meteorological supersite for aviation and cold weather applications. *Pure and Applied Geophysics*, 176, 1977–2015.
- Gultepe, I., Heymsfield, A.J., Fernando, H.J.S., Pardyjak, E., Dorman, C.E., Wang, Q. et al. (2021) A review of coastal fog microphysics during c-fog. *Boundary-Layer Meteorology*, 181, 227–265.
- Gultepe, I. & Isaac, G.A. (1997) Liquid water content and temperature relationship from aircraft observations and its applicability to gcms. *Journal of Climate*, 10, 446–452.
- Gultepe, I., Tardif, R., Michaelides, S.C., Cermak, J., Bott, A., Bendix, J. et al. (2007) Fog research: a review of past achievements and future perspectives. *Pure Applied Geophysics*, 164, 1121–1159.
- Hanna, S.R. (1987) An empirical formula for the height of the coastal internal boundary layer. *Boundary-Layer Meteorology*, 40, 205–207.
- Hodur, R.M. (1997) The naval research laboratory’s coupled ocean/atmosphere mesoscale prediction system (coamps). *Monthly Weather Review*, 125, 1414–1430.
- Jackson, N.A. (1976) The propagation of modified flow downstream of a change in roughness. *Quarterly Journal of the Royal Meteorological Society*, 102, 924–933.
- Kaimal, J.C. & Finnigan, J.J. (1994) *Atmospheric boundary layer flows: their structure and measurements*. Oxford: Oxford University Press.
- Kim, C.K. & Yum, S.S. (2012) A numerical study of sea-fog formation over cold sea surface using a one-dimensional turbulence model coupled with the weather research and forecasting model. *Boundary-Layer Meteorology*, 143, 481–505.
- Krishnamurthy, R., Fernando, H.J.S., Alappattu, D., Creegan, E. & Wang, Q. (2023) Observations of offshore internal boundary layers. *Journal of Geophysical Research: Atmospheres*, 128, e2022JD037425.
- Lee, T.F. (1987) Urban clear islands in california central valley fog. *Monthly Weather Review*, 115, 1794–1796.
- Lenain, L. & Melville, W.K. (2014) Autonomous surface vehicle measurements of the ocean’s response to tropical cyclone freda. *Journal of Atmospheric and Oceanic Technology*, 31, 2169–2190.
- Mahrt, L. (2000) Surface heterogeneity and vertical structure of the boundary layer. *Boundary-Layer Meteorology*, 96, 33–62.
- Mahrt, L. & Vickers, D. (2004) Bulk formulation of the surface heat flux. *Boundary-Layer Meteorology*, 110, 357–379.
- Mauder, M., Foken, T. & Cuxart, J. (2020) Surface-energy-balance closure over land: a review. *Boundary-Layer Meteorology*, 177, 395–426.
- Miyake, M. (1965) *Transformation of the atmospheric boundary layer over inhomogeneous surfaces*. Seattle, WA: Univ. of Washington
- Monin, A.S. & Yaglom, A.M. (1971) *Statistical Fluid Mechanics: Mechanics of Turbulence*, Vol. 1.
- Mulhearn, P.J. (1977) Relations between surface fluxes and mean profiles of velocity, temperature and concentration, downwind of a change in surface roughness. *Quarterly Journal of the Royal Meteorological Society*, 103, 785–802.
- O’Brien, T.A., Sloan, L.C., Chuang, P.Y., Faloona, I.C. & Johnstone, J.A. (2013) Multidecadal simulation of coastal fog with a regional climate model. *Climate Dynamics*, 40, 2801–2812.
- Onishi, G. & Estoque, M.A. (1968) Numerical study on atmospheric boundary layer flow over inhomogeneous terrain. *Journal of the Meteorological Society of Japan*, 46, 280–286.
- Ortiz-Suslow, D., Kalogiros, J., Fernando, H., Creegan, E., Pardyjak, E., Gaberšek, S. et al. (2024) A case study of boundary layer development downstream of a small maritime Island. *Quarterly Journal of the Royal Meteorological Society*.
- Pagowski, M., Gultepe, I. & King, P. (2004) Analysis and modeling of an extremely dense fog event in southern ontario. *Journal of Applied Meteorology*, 43, 3–16.
- Panofsky, H.A. (1973) Tower micrometeorology. In: *Workshop on micrometeorology*, Vol. 151. Boston, MA: American Meteorological Society, p. 176.
- Panofsky, H.A. & Dutton, J.A. (1984) *Atmospheric turbulence. Models and methods for engineering applications*. New York: Wiley.
- Panofsky, H.A. & Townsend, A.A. (1964) Change of terrain roughness and the wind profile. *Quarterly Journal of the Royal Meteorological Society*, 90, 147–155.
- Pendergrass, W. & Arya, S.P.S. (1984) Dispersion in neutral boundary layer over a step change in surface roughness - i. mean flow and turbulence structure. *Atmospheric Environment*, 18, 1267–1279.
- Radikevitch, V.M. (1971) Transformazija dinamičeskikh karakteristik vozdušnogo potoka pod vlijanjem izmenenija šeročovatosti podstila justsčej poverchnosti. *Izvestia AN SSSR, Fizika Atmosfery i Okeana*, 7, 1241–1250.
- Rodhe, B. (1962) The effect of turbulence on fog formation. *Tellus*, 14, 49–86.
- Ryznar, E. (1977) Advection-radiation fog near lake michigan. *Atmospheric Environment*, 11, 427–430.
- Sachweh, M. & Koepke, P. (1995) Radiation fog and urban climate. *Geophysical Research Letters*, 22, 1073–1076.
- Savelyev, S.A. & Taylor, P.A. (2001) Notes on an internal boundary-layer height formula. *Boundary-Layer Meteorology*, 101, 293–301.
- Savelyev, S.A. & Taylor, P.A. (2005) Internal boundary layers: I. Height formulae for neutral and diabatic flows. *Boundary-Layer Meteorology*, 115, 1–25.
- Schimmel, G., Produit, T., Mongin, D., Kasparian, J. & Wolf, J.P. (2018) Free space laser telecommunication through fog. *Optica*, 5, 1338–1341.
- Schofield, W.H. (1975) Measurements in adverse-pressure-gradient turbulent boundary layers with a step change in surface roughness. *Journal of Fluid Mechanics*, 70, 573–593.

- Shir, C.C. (1972) A numerical computation of air flow over a sudden change of surface roughness. *Journal of Atmospheric Sciences*, 29, 304–310.
- Smith, S.D. (1988) Coefficients for sea surface wind stress, heat flux, and wind profiles as a function of wind speed and temperature. *Journal of Geophysical Research: Oceans*, 93, 15467–15472.
- Sorbjan, Z. (1989) Structure of the Atmospheric Boundary Layer. No. 551.51 SOR.
- Stull, R.B. (1988) *An introduction to boundary layer meteorology*, Vol. 13. Dordrecht, Netherlands: Springer Science & Business Media.
- Taylor, G.I. (1917) The formation of fog and mist. *Quarterly Journal of the Royal Meteorological Society*, 43, 241–268.
- Townsend, A.A. (1965) The response of a turbulent boundary layer to abrupt changes in surface conditions. *Journal of Fluid Mechanics*, 22, 799–822.
- Townsend, A.A. (1966) The flow in a turbulent boundary layer after a change in surface roughness. *Journal of Fluid Mechanics*, 26, 255–266.
- Townsend, A.A. (1976) *The structure of turbulent shear flow*. Cambridge, UK: Cambridge university press.
- Underwood, S.J. & Hansen, C. (2008) Investigating urban clear islands in fog and low stratus clouds in the san joaquin valley of california. *Physical Geography*, 29, 442–454.
- WMO. (1992) International meteorological vocabulary.
- Wood, D.H. (1982) Internal boundary layer growth following a step change in surface roughness. *Boundary-Layer Meteorology*, 22, 241–244.
- Wyngaard, J.C. (2010) *Turbulence in the atmosphere*. New York: Cambridge University Press.
- Yan, S., Zhu, B., Huang, Y., Zhu, J., Kang, H., Lu, C. et al. (2020) To what extents do urbanization and air pollution affect fog? *Atmospheric Chemistry and Physics*, 20, 5559–5572.
- Zilitinkevich, S.S., Tyuryakov, S.A., Troitskaya, Y.I. & Mareev, E.A. (2012) Theoretical models of the height of the atmospheric boundary layer and turbulent entrainment at its upper boundary. *Izvestiya, Atmospheric and Oceanic Physics*, 48, 133–142.

How to cite this article: Bardoel, S.L., Hoch, S., Ruiz-Plancarte, J., Lenain, L., Gultepe, I., Grachev, A.A. et al. (2024) Study of fog dissipation in an internal boundary layer on Sable Island. *Quarterly Journal of the Royal Meteorological Society*, 1–23. Available from: <https://doi.org/10.1002/qj.4891>